SIAM J. SCI. COMPUT.
Vol. 28, No. 2, pp. 533–560

NONOSCILLATORY CENTRAL SCHEMES FOR ONE- AND TWO-DIMENSIONAL MAGNETOHYDRODYNAMICS EQUATIONS. II: HIGH-ORDER SEMIDISCRETE SCHEMES*

JORGE BALBÁS† AND EITAN TADMOR‡

Abstract. We present a new family of high-resolution, nonoscillatory semidiscrete central schemes for the approximate solution of the ideal magnetohydrodynamics (MHD) equations. This is the second part of our work, where we are passing from the fully discrete staggered schemes in [J. Balbás, E. Tadmor, and C.-C. Wu, *J. Comput. Phys.*, 201 (2004), pp. 261–285] to the semidiscrete formulation advocated in [A. Kurganov and E. Tadmor, *J. Comput. Phys.*, 160 (2000), pp. 241–282]. This semidiscrete formulation retains the simplicity of fully discrete central schemes while enhancing efficiency and adding versatility. The semidiscrete algorithm offers a wider range of options to implement its two key steps: nonoscillatory reconstruction of point values followed by the evolution of the corresponding point valued fluxes. We present the solution of several prototype MHD problems. Solutions of one-dimensional Brio–Wu shock-tube problems and the two-dimensional Kelvin–Helmholtz instability, Orszag–Tang vortex system, and the disruption of a high density cloud by a strong shock are carried out using third- and fourth-order central schemes based on the central WENO reconstructions. These results complement those presented in our earlier work and confirm the remarkable versatility and simplicity of central schemes as black-box, Jacobian-free MHD solvers. Furthermore, our numerical experiments demonstrate that this family of semidiscrete central schemes preserves the $\nabla \cdot \mathbf{B} = 0$-constraint within machine round-off error; happily, no constrained-transport enforcement is needed.

Key words. multidimensional conservation laws, ideal magnetohydrodynamics (MHD) equations, high-resolution central schemes, nonoscillatory reconstructions, Jacobian-free form, semi-discrete schemes

AMS subject classifications. Primary 65M10; Secondary 65M05, 76W05

DOI. 10.1137/040610246

1. Introduction.

In this paper we present third- and fourth-order accurate, nonoscillatory semidiscrete central schemes for the approximate solution of the equations of ideal magnetohydrodynamics,

$$\rho_t = -\nabla \cdot (\rho \mathbf{v}), \tag{1.1}$$

$$(\rho \mathbf{v})_t = -\nabla \cdot \left[\rho \mathbf{v}\mathbf{v}^\top + \left(p + \frac{1}{2} B^2 \right) I_{3\times 3} - \mathbf{B}\mathbf{B}^\top \right], \tag{1.2}$$

$$\mathbf{B}_t = \nabla \times (\mathbf{v} \times \mathbf{B}), \tag{1.3}$$

$$e_t = -\nabla \cdot \left[\left(\frac{\gamma}{\gamma - 1} p + \frac{1}{2} \rho v^2 \right) \mathbf{v} - (\mathbf{v} \times \mathbf{B}) \times \mathbf{B} \right]. \tag{1.4}$$

Here, ρ and e are scalar quantities representing, respectively, the mass density and the total internal energy, $\mathbf{v} = (v_x, v_y, v_z)^\top$ is the velocity field with *Euclidean* norm

*Received by the editors June 20, 2004; accepted for publication (in revised form) October 17, 2005; published electronically April 21, 2006. This research was supported in part by NSF grant 04-07704 and ONR grant N00014-91-J-1076.

http://www.siam.org/journals/sisc/28-2/61024.html.

†Department of Mathematics, University of Michigan, Ann Arbor, MI 48109 (jbalbas@umich.edu). Part of the research was carried out while this author was visiting the Center for Scientific Computation and Mathematical Modeling (CSCAMM) at the University of Maryland, College Park. Research was supported in part by an NSF VIGRE grant.

‡Department of Mathematics, Center of Scientific Computation and Mathematical Modeling (CSCAMM) and Institute for Physical Science and Technology (IPST), University of Maryland, College Park, MD 20742 (tadmor@cscamm.umd.edu).

$v^2 := \|\mathbf{v}\|^2$, and $\mathbf{B} = (B_x, B_y, B_z)^\top$ and $B^2 := \|\mathbf{B}\|^2$ represent the magnetic field and its norm. The pressure, p, is coupled to the internal energy, $e = \frac{1}{2}\rho v^2 + \frac{1}{2}B^2 + p/(\gamma - 1)$, where γ is the (fixed) ratio of specific heats. The system is augmented by the solenoidal constraint,

$$\nabla \cdot \mathbf{B} = 0; \tag{1.5}$$

that is, if the condition $\nabla \cdot \mathbf{B} = 0$ is satisfied initially at $t = 0$, then by (1.3) it remains invariant in time.

Our work [2] demonstrated the capability of central schemes to accurately and efficiently detect and resolve the steep gradients that characterize the solutions of (1.1)–(1.4); it suggested further development of higher-order, black-box-type central schemes for these equations. In this paper, we present a family of third- and fourth-order accurate, nonoscillatory semidiscrete central schemes which remain stable without any further explicit enforcement of the constraint (1.5). This semidiscrete formulation [14] retains the main advantages of central schemes over the upwind ones, namely, simplicity and efficiency resulting from the minimal amount of characteristic information required when evolving the solution over staggered grids, allowing for Jacobian-free formulations and avoiding dimensional splitting in multidimensional models. Moreover, semidiscrete schemes allow more flexibility in the calculation of the time step, Δt, than their fully discrete counterparts: on the one hand, they are implemented over nonstaggered grids, and thus the CFL stability condition allows for the use of larger time steps, and on the other hand, for rth-order methods, the numerical dissipation of the semidiscrete formulation is of order $\mathcal{O}((\Delta x)^{2r-1})$ versus that of the corresponding fully discrete version of order $\mathcal{O}((\Delta x)^{2r}/\Delta t)$, which allows the use of smaller time steps with considerably less smearing of discontinuities. Finally, the semidiscrete formulation also enjoys a remarkable adaptability to a wide range of nonoscillatory reconstruction techniques and evolution routines developed independently of the methods.

In addition to the five magnetohydrodynamics (MHD) prototype problems discussed in [2]—two one-dimensional Brio and Wu shock tube models originally proposed in [3], two different configurations (periodic and convective models) of the two-dimensional transverse Kelvin–Helmholtz instability problem, and the two-dimensional MHD vortex system of Orszag and Tang—we implement these new schemes to simulate the disruption of a high density cloud by a strong shock. The evolution of the Orszag–Tang vortex system involves the interaction between several shock waves traveling at various speed regimes, and the interaction between the high-density cloud and the strong shock describes a highly superfast flow, making both of these very suitable problems to test the robustness of numerical algorithms.

The paper is structured as follows. In section 2, we extend the derivation of the second- and third-order, central semidiscrete schemes presented in [14, 13, 12] to schemes of arbitrary order r. Starting with the staggered discretization that led to the fully discrete central schemes [20, 19, 10, 17], we evolve separately the smooth and nonsmooth parts of the solution and project the resulting cell averages back onto the original grid. We then pass to the $\Delta t \downarrow 0$-limit, yielding the rth-order semidiscrete formulation of central schemes. This rather general formulation of central schemes entertains a broad range of options to implement the two main steps of the algorithm: nonoscillatory *reconstruction* of point values from cell averages, followed by the *evolution* of the corresponding point valued fluxes. In section 3 we discuss the nonoscillatory reconstruction techniques and evolution routines that we implement to approximate

the semidiscrete formulation of (1.1)–(1.4). For the reconstruction of point values, we propose an extension of the third-order central WENO (CWENO) reconstruction of Kurganov and Levy [12] and the *genuinely* two-dimensional fourth-order CWENO reconstruction of Levy, Puppo, and Russo [18], developed originally in the context of fully discrete central schemes. For the evolution step, we use third- and fourth-order strong stability preserving (SSP) Runge–Kutta schemes [23, 25, 5]. In sections 4 and 5 we describe the prototype MHD problems mentioned above and present the numerical solutions obtained with our new family of high-resolution semidiscrete central schemes. In section 4 we report on the one-dimensional shock tube problems of Brio and Wu [3] and discuss the improved resolution and better control of spurious oscillations provided by the new schemes. The two-dimensional test problems and the corresponding numerical results are presented and discussed in section 5. These results confirm the efficiency of central schemes to accurately compute the solution of MHD equations. The combination of simplicity and high resolution allows us to obtain solutions comparable to those obtained with high-order upwind schemes, e.g., [3, 4, 11, 22, 21], without having to refine the computational mesh as in [2]. We therefore retain the simplicity of central schemes—they eliminate the need for a detailed knowledge of the eigen-structure of the Jacobian matrices and avoid dimensional splitting and the costly use of (approximate) Riemann solvers that serve as building blocks for upwind schemes; at the same time, this simplicity is achieved without an increase in the computational work that was enforced by the finer meshes required with the lower-order methods and/or any explicit enforcement of the solenoidal constraint $\nabla \cdot \mathbf{B} = 0$.

2. Semidiscrete central schemes. In [2] we demonstrated the robustness of black-box-type central schemes to calculate the approximate solutions of (1.1)–(1.4) and discussed the advantages of these methods over those based on upwind differencing. We also pointed out, however, that the efficiency resulting from a minimal amount of characteristic information required by central schemes may be compromised by the low-order accuracy of the schemes, since the latter often require finer meshes to resolve steep gradients. In order to circumvent this limitation and gain full advantage of the simplicity, ease of implementation, and efficiency of central schemes, we seek higher-order methods. Although it is possible to carry out a higher-order extension of the fully discrete central schemes discussed in [2] (see, e.g., [16, 18]), we find the semidiscrete formulation of Kurganov and Tadmor [14] more advantageous: its implementation over nonstaggered grids allows the use of larger time steps, it enjoys a reduced numerical dissipation (of order $\mathcal{O}((\Delta x)^{2r-1})$) in comparison to that of fully discrete schemes ($\sim \mathcal{O}((\Delta x)^{2r}/\Delta t)$), and it is derived independently of any reconstruction or evolution algorithm. Indeed, many of the existing high-order, nonoscillatory reconstruction algorithms and evolution routines can be easily incorporated into the semidiscrete central formulation, making the simplicity and ease of implementation of central schemes an attractive alternative.

2.1. One-dimensional schemes. The solutions of nonlinear hyperbolic systems of conservation laws,

$$u_t + f(u)_x = 0, \tag{2.1}$$

and in particular those of (1.1)–(1.4), are characterized by the onset and propagation of discontinuities. The higher-order extensions of the first-order Lax–Friedrichs central scheme [15] that have been developed over the past two decades (see, e.g., [20, 19,

10, 14]) provide a rather general approach for solving this type of problem with only a minimal amount of information on the eigen structure of the Jacobian matrix of $f(u)$. (Indeed, Jacobian-free formulations of central schemes completely avoid the computation of $\frac{\partial f}{\partial u}$.) These schemes are based on the evolution of the cell averages (we use the usual $\fint_I$ to denote the average, $1/|I| \cdot \int_I$),

$$\bar{u}_\alpha^n := \fint_{I_\alpha} u(\xi, t^n) d\xi, \qquad I_\alpha := \left[x_\alpha - \frac{\Delta x}{2}, x_\alpha + \frac{\Delta x}{2} \right],$$

while alternating over *staggered* grids, $\{I_j\} \times t^n$ and $\{I_{j+\frac{1}{2}}\} \times t^{n+1}$. Dividing (2.1) by Δx and integrating over the control volume $I_{j+\frac{1}{2}} \times [t^n, t^{n+1}]$ yields an exact discrete statement of the conservation law in terms of these cell averages,

$$\bar{u}_{j+\frac{1}{2}}^{n+1} = \bar{u}_{j+\frac{1}{2}}^n - \frac{1}{\Delta x} \left[\int_{t^n}^{t^{n+1}} f(u(x_{j+1}, \tau)) d\tau - \int_{t^n}^{t^{n+1}} f(u(x_j, \tau)) d\tau \right]. \tag{2.2}$$

The evaluation of the expressions on the right of (2.2) proceeds in two steps. First, the cell averages $\{\bar{u}_{j+\frac{1}{2}}^n\}$ are recovered by integrating a piecewise nonoscillatory polynomial reconstruction of the point-values of $u(x, t^n)$ from their cell averages $\{\bar{u}_j^n\}$ that we denote by

$$u(x, t^n) = R\,(x; \bar{u}^n) := \sum_j p_j^n(x) \cdot \mathbf{1}_{I_j}. \tag{2.3}$$

This reconstruction procedure is at the heart of high-resolution, nonoscillatory central schemes and requires the coefficients of the polynomials $\{p_j^n(x)\}$ to be determined so that $R(x; \bar{u}^n)$ satisfies the following three essential properties:

- $\mathcal{P}_1$—conservation of cell averages: $\bar{p}_j^n(x) = \bar{u}_j^n$.
- $\mathcal{P}_2$—accuracy: $R\,(x; \bar{u}^n) = u(x, t^n) + \mathcal{O}((\Delta x)^r)$ for rth-order accurate scheme, wherever $u(\cdot, t^n)$ is sufficiently smooth.
- $\mathcal{P}_3$—nonoscillatory behavior of $\sum_j p_j(x) \cdot \mathbf{1}_{I_j}$ which is characterized in different ways for different reconstructions. Examples include TVD reconstructions initiated by van Leer [27] and Harten [7], number of extrema diminishing (NED) and shape-preserving properties of the Liu–Tadmor third-order scheme [19], and the higher-order nonoscillatory extensions offered by the essentially nonoscillatory (ENO) reconstructions of Harten et al. [6] or their weighted versions (WENO), e.g., [24, 9], and their implementation within the central differencing framework, e.g., [12, 16, 18].

Equipped with the reconstructed point values $u(\cdot, t^n)$, the second step evaluates the two time integrals of $f(u(\cdot, \tau))$. Since the solution of (2.2) remains smooth along the lines $\{x = x_j\} \times [t^n, t^{n+1}]$, a simple quadrature rule suffices to approximate those integrals. This requires the intermediate values, $\{\bar{u}_j^{n+\beta}\}$, which are predicted either by a Taylor expansion or alternatively by Runge–Kutta solvers of the ODE $u_\tau = \hat{f}_x|_{x=x_j}$, $u(x_j, 0) = u_j^n$, $\tau > t^n$, where $\hat{f}_x$ stands for the numerical derivative of $f(u)$. This type of evolution over staggered grids based on cells with uniform width Δx does not admit a semidiscrete limit as $\Delta t \downarrow 0$. Instead, a modified approach proposed by Kurganov and Tadmor in [14] and based on variable size cells (depicted in Figure 2.1) yields the desired semidiscrete limit. Here, we extend the derivation of second- and third-order semidiscrete schemes of [14, 12, 13] to schemes of arbitrary order of accuracy r [1]. The first step passing from a fully discrete to a semidiscrete formulation consists of

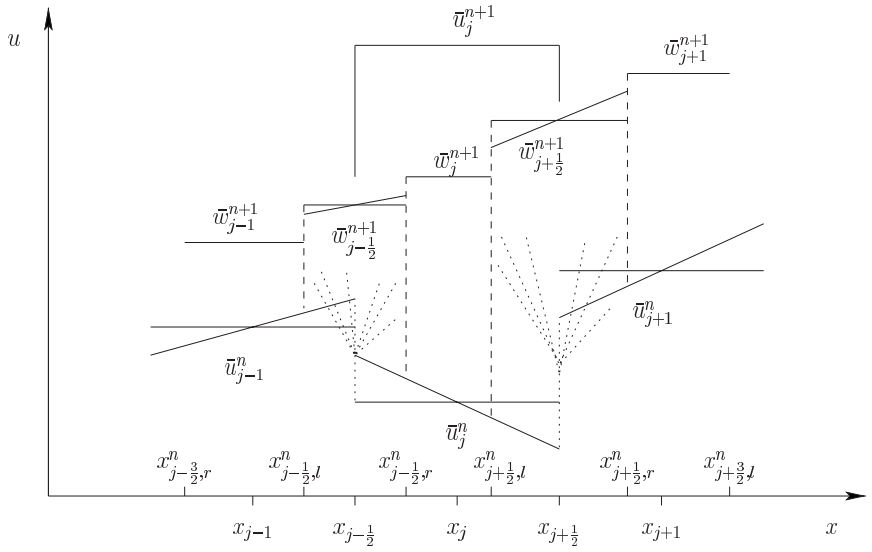

FIG. 2.1. *Modified central differencing of Kurganov and Tadmor.*

reducing the size of the staggered cells covering the Riemann fans. Instead of cells with uniform width Δx, we use cells with variable width of order $\mathcal{O}(\Delta t)$, by incorporating the maximal local speed of propagation,

$$a_{j+\frac{1}{2}}^n = \max_{u\in\mathcal{C}\left(u_{j+\frac{1}{2}}^-,u_{j+\frac{1}{2}}^+\right)} \rho\left(\frac{\partial f}{\partial u}(u)\right); \tag{2.4}$$

here $u_{j+\frac{1}{2}}^-$ and $u_{j+\frac{1}{2}}^+$ stand for, respectively, the reconstructed values of u to the left and right of the interfacing breakpoints, $u_{j+\frac{1}{2}}^{\pm} := R(x_{j+\frac{1}{2}}\pm, \bar{u}^n)$, and $\mathcal{C}$ is the phase curve connecting these two states through the Riemann fan. For practical purposes, we choose

$$a_{j+\frac{1}{2}}^n := \max\left\{\rho\left(\frac{\partial f}{\partial u}(u_{j+\frac{1}{2}}^-)\right), \rho\left(\frac{\partial f}{\partial u}(u_{j+\frac{1}{2}}^+)\right)\right\},$$

which is exact for genuinely nonlinear and linearly degenerate fields.

This information allows us to repartition the original grid so as to distinguish between subcells of width $2a_{j+\frac{1}{2}}^n\Delta t^n$, where the solution is dictated by the nonsmooth Riemann fan,

$$\widetilde{I}_{j+\frac{1}{2}} = \left[x_{j+\frac{1}{2},l}^n,\ x_{j+\frac{1}{2},r}^n\right] := \left[x_{j+\frac{1}{2}} - a_{j+\frac{1}{2}}^n\Delta t^n,\ x_{j+\frac{1}{2}} + a_{j+\frac{1}{2}}^n\Delta t^n\right],$$

and the other cells of width $\Delta x_j := \Delta x - \Delta t^n(a_{j-\frac{1}{2}}^n + a_{j+\frac{1}{2}}^n)$, which are beyond the influence of the Riemann fans so that the solution remains smooth,

$$\widetilde{I}_j = \left[x_{j-\frac{1}{2},r}^n,\ x_{j+\frac{1}{2},l}^n\right] := \left[x_{j-\frac{1}{2}} + a_{j-\frac{1}{2}}^n\Delta t^n,\ x_{j+\frac{1}{2}} - a_{j+\frac{1}{2}}^n\Delta t^n\right].$$

In nonsmooth regions, the cell averages $\{\bar{w}^{n+1}_{j+\frac{1}{2}}\}$ are computed via staggered evolution over the (narrower, $\mathcal{O}(\Delta t)$) cells covering the Riemann fans,

$$\begin{aligned}\bar{w}^{n+1}_{j+\frac{1}{2}} &:= \fint_{x^n_{j+\frac{1}{2},l}}^{x^n_{j+\frac{1}{2},r}} u(x,t^{n+1})dx \\ &= \fint_{x^n_{j+\frac{1}{2},l}}^{x^n_{j+\frac{1}{2},r}} R\,(x;\bar{u}^n)dx - \frac{1}{2a^n_{j+\frac{1}{2}}}\int_{t^n}^{t^{n+1}} \big[f(u(x^n_{j+\frac{1}{2},r},\tau)) - f(u(x^n_{j+\frac{1}{2},l},\tau))\big]d\tau, \end{aligned} \tag{2.5}$$

and in the smooth regions, direct integration of (2.1) yields the cell averages $\{\bar{w}^n_j\}$

$$\begin{aligned}\bar{w}^{n+1}_{j} &:= \fint_{x^n_{j-\frac{1}{2},r}}^{x^n_{j+\frac{1}{2},l}} u(x,t^{n+1})dx \\ &= \fint_{x^n_{j-\frac{1}{2},r}}^{x^n_{j+\frac{1}{2},l}} R\,(x;\bar{u}^n)dx - \frac{1}{\Delta x_j}\int_{t^n}^{t^{n+1}} \big[f(u(x^n_{j+\frac{1}{2},l},\tau)) - f(u(x^n_{j-\frac{1}{2},r},\tau))\big]d\tau. \end{aligned} \tag{2.6}$$

The *nonstaggered* cell averages, $\{\bar{u}^{n+1}_j\}$, are then recovered via a new nonoscillatory piecewise polynomial reconstruction of the point values of $u(x,t^{n+1})$ from the new cell averages (2.5) and (2.6),

$$R\,(x;\bar{w}^{n+1}) = \sum_j q^{n+1}_j(x)\cdot \mathbf{1}_{\widetilde{I}_j} + q^{n+1}_{j+\frac{1}{2}}(x)\cdot \mathbf{1}_{\widetilde{I}_{j+\frac{1}{2}}}. \tag{2.7}$$

Projection onto the original grid, $\{I_j\}$, (2.7) yields

$$\begin{aligned}\bar{u}^{n+1}_j &:= \fint_{x_{j-\frac{1}{2}}}^{x_{j+\frac{1}{2}}} R\,(x;\bar{w}^{n+1})dx \\ &= \frac{1}{\Delta x}\left[\int_{x_{j-\frac{1}{2}}}^{x_{j-\frac{1}{2},r}} q^{n+1}_{j-\frac{1}{2}}(x)\,dx + \int_{x_{j-\frac{1}{2},r}}^{x_{j+\frac{1}{2},l}} q^{n+1}_{j}(x)\,dx + \int_{x_{j+\frac{1}{2},l}}^{x_{j+\frac{1}{2}}} q^{n+1}_{j+\frac{1}{2}}(x)\,dx\right]. \end{aligned} \tag{2.8}$$

The explicit calculation of the polynomials $q^{n+1}_j(x)$ and $q^{n+1}_{j+1/2}(x)$ will, in fact, prove to be irrelevant for the semidiscrete formulation that we seek. As we shall see below, only the *cell averages* of these q's matter, and in the $\Delta t \downarrow 0$-limit, these averages are further reduced to the original point values reconstructed at the interfaces, $p(x_{j\pm\frac{1}{2}},t^n)$. We turn to the details. Without loss of generality, we assume that the q^{n+1} are polynomials of degree $r-1$ (required to preserve the underlying rth-order accuracy) and satisfy properties $\mathcal{P}_1$ – $\mathcal{P}_3$ for the cell averages (2.5) and (2.6) in the corresponding cells $\widetilde{I}_j$ and $\widetilde{I}_{j+\frac{1}{2}}$. We express these polynomials as $q^{n+1}_{j\pm\frac{1}{2}}(x) = \sum_{k=0}^{r-1} A^{(k)}_{j\pm\frac{1}{2}}(x - x_{j\pm\frac{1}{2}})^k/k!$; their coefficients can be uniquely determined by imposing the conservation constraints,[1]

$$\fint_{\widetilde{I}_{j+p}} q^{n+1}_{j+s}(x)dx = \bar{w}^n_{j+p}, \qquad p = 0, \pm\frac{1}{2}, \pm 1, \ldots, \pm\frac{r-1}{2}, \qquad s = -\frac{1}{2}, 0, \frac{1}{2}. \tag{2.9}$$

[1]The choice of symmetric intervals around $\tilde{I}_j$ yields methods of odd order. For methods of even order, it suffices to sacrifice one of the side constraints, $p = \pm\frac{r-1}{2}$.

Equipped with this notation, the first and last integrals on the right of (2.8) read

$$\begin{aligned}\int_{x_{j-\frac{1}{2}}}^{x_{j-\frac{1}{2},r}} q_{j-\frac{1}{2}}^{n+1}(x)\,dx &= \sum_{k=0}^{r-1}\left[\frac{A_{j-\frac{1}{2}}^{(k)}}{(k+1)!}(x-x_{j-\frac{1}{2}})^{k+1}\right]_{x_{j-\frac{1}{2}}}^{x_{j-\frac{1}{2}}+a_{j-\frac{1}{2}}^{n}\Delta t}\\ &= \sum_{k=0}^{r-1}\frac{(\Delta t)^{k+1}}{(k+1)!}(a_{j-\frac{1}{2}}^{n})^{k+1}A_{j-\frac{1}{2}}^{(k)}\end{aligned} \tag{2.10}$$

and

$$\begin{aligned}\int_{x_{j+\frac{1}{2},l}}^{x_{j+\frac{1}{2}}} q_{j+\frac{1}{2}}^{n+1}(x)\,dx &= \sum_{k=0}^{r-1}\left[\frac{A_{j+\frac{1}{2}}^{(k)}}{(k+1)!}(x-x_{j+\frac{1}{2}})^{k+1}\right]_{x_{j+\frac{1}{2}}-a_{j+\frac{1}{2}}^{n}\Delta t}^{x_{j+\frac{1}{2}}}\\ &= \sum_{k=0}^{r-1}(-1)^{k}\frac{(\Delta t)^{k+1}}{(k+1)!}(a_{j+\frac{1}{2}}^{n})^{k+1}A_{j+\frac{1}{2}}^{(k)}.\end{aligned} \tag{2.11}$$

For the second integral in (2.8), we observe that by property $\mathcal{P}_1$ the polynomial $q_j^{n+1}(x)$ must satisfy

$$\int_{x_{j-\frac{1}{2}},r}^{x_{j+\frac{1}{2}},l} q_j^{n+1}(x)\,dx = \Delta x_j \bar{w}_j^{n+1} = \left[\Delta x - \Delta t(a_{j-\frac{1}{2}}^{n} + a_{j+\frac{1}{2}}^{n})\right]\bar{w}_j^{n+1}. \tag{2.12}$$

Substituting (2.10)–(2.12) into (2.8), we arrive at a fully discrete, nonstaggered approximation (of arbitrary order of accuracy r) of the cell averages in (2.2),

$$\begin{aligned}\bar{u}_j^{n+1} = &\sum_{k=0}^{r-1}\frac{\lambda(\Delta t)^k}{(k+1)!}\left[(a_{j-\frac{1}{2}}^{n})^{k+1}A_{j-\frac{1}{2}}^{(k)} + (-1)^k(a_{j+\frac{1}{2}}^{n})^{k+1}A_{j+\frac{1}{2}}^{(k)}\right]\\ &+ \left[1-\lambda(a_{j-\frac{1}{2}}^{n} + a_{j+\frac{1}{2}}^{n})\right]\bar{w}_j^{n+1}, \quad \lambda := \frac{\Delta t}{\Delta x}.\end{aligned} \tag{2.13}$$

Given the appropriate reconstructions $R(x;\bar{u}^n)$, $R(x;\bar{w}^n)$ and quadrature rules to evaluate the flux integrals in (2.5) and (2.6), then (2.13) constitutes a family of fully discrete nonoscillatory central schemes, e.g., [8, 14]. This type of scheme admits a considerably simpler and more versatile semidiscrete limit, $d\bar{u}_j/dt := \lim_{\Delta t\to 0}(\bar{u}_j(t^n+\Delta t) - \bar{u}_j(t^n))/\Delta t$.

To this end, we rewrite (2.13) as

$$\begin{aligned}\frac{d\bar{u}_j}{dt} = &\lim_{\Delta t\to 0}\left\{\frac{1}{\Delta x}\left(a_{j-\frac{1}{2}}^{n}A_{j-\frac{1}{2}}^{(0)} + a_{j+\frac{1}{2}}^{n}A_{j+\frac{1}{2}}^{(0)}\right) + \frac{1}{\Delta t}(\bar{w}_j^{n+1} - \bar{u}_j^{n})\right.\\ &- \frac{1}{\Delta x}\left(a_{j-\frac{1}{2}}^{n} + a_{j+\frac{1}{2}}^{n}\right)\bar{w}_j^{n+1} + \sum_{k=1}^{r-1}\frac{\lambda(\Delta t)^{k-1}}{(k+1)!}\left[\left(a_{j-\frac{1}{2}}^{n}\right)^{k+1}A_{j-\frac{1}{2}}^{(k)}\right.\\ &\left.\left.+ (-1)^k\left(a_{j+\frac{1}{2}}^{n}\right)^{k+1}A_{j+\frac{1}{2}}^{(k)}\right]\right\}\\ = &\lim_{\Delta t\to 0}\left\{\frac{1}{\Delta x}\left(a_{j-\frac{1}{2}}^{n}A_{j-\frac{1}{2}}^{(0)} + a_{j+\frac{1}{2}}^{n}A_{j+\frac{1}{2}}^{(0)}\right) + \frac{1}{\Delta t}(\bar{w}_j^{n+1} - \bar{u}_j^{n})\right.\\ &\left.- \frac{1}{\Delta x}\left(a_{j-\frac{1}{2}}^{n} + a_{j+\frac{1}{2}}^{n}\right)\bar{w}_j^{n+1}\right\}.\end{aligned} \tag{2.14}$$

Since the width of the local Riemann fans approaches zero in the $\Delta t \downarrow 0$-limit, i.e., $x^n_{j+\frac{1}{2},l}, x^n_{j+\frac{1}{2},r} \to x_{j+\frac{1}{2}}$, we obtain by conservation of cell averages property $\mathcal{P}_1$, $A^{(0)}_{j\pm\frac{1}{2}} = \bar{w}^{n+1}_{j\pm\frac{1}{2}}$ so that (2.14) yields

$$\begin{aligned}\frac{d\bar{u}_j}{dt} = \lim_{\Delta t\to 0}\Bigg\{ &\frac{1}{\Delta x}\left(a^n_{j-\frac{1}{2}}\bar{w}^{n+1}_{j-\frac{1}{2}} + a^n_{j+\frac{1}{2}}\bar{w}^{n+1}_{j+\frac{1}{2}}\right) + \frac{1}{\Delta t}(\bar{w}^{n+1}_j - \bar{u}^n_j)\\ &- \frac{1}{\Delta x}\left(a^n_{j-\frac{1}{2}} + a^n_{j+\frac{1}{2}}\right)\bar{w}^{n+1}_j\Bigg\}.\end{aligned} \tag{2.15}$$

As $\Delta t \downarrow 0$ we end up with limiting values which depend solely on the reconstructed values $R(x,u)$ on both sides of the interfacing breakpoints, $x_{j\pm\frac{1}{2}}$, given by

$$\begin{aligned} u(x^n_{j+\frac{1}{2},l}, t) &\to p^n_j(x_{j+\frac{1}{2}}) =: u^-_{j+\frac{1}{2}}(t),\\ u(x^n_{j+\frac{1}{2},r}, t) &\to p^n_{j+1}(x_{j+\frac{1}{2}}) =: u^+_{j+\frac{1}{2}}(t);\end{aligned} \tag{2.16}$$

here $p^n_j(x)$ and $p^n_{j+1}(x)$ are the polynomial reconstructions of $R(x;\bar{u}^n)$ at the original time step t^n introduced in (2.3). The corresponding averages in (2.5) approach $\bar{w}^{n+1}_{j+\frac{1}{2}} \sim (\Delta f)_{j+\frac{1}{2}}/2a^n_{j+\frac{1}{2}}$, where $(\Delta f)_{j+\frac{1}{2}} := f(u^+_{j+\frac{1}{2}}) - f(u^-_{j+\frac{1}{2}})$, while the smoother averages in (2.6) are of order $\bar{w}^{n+1}_j \sim \bar{u}^n_j - \Delta t(\Delta f)_{j+\frac{1}{2}}$. Inserted into (2.15), we end up with a semidiscrete limit which can be written in its final conservative form,

$$\frac{d\bar{u}_j}{dt} = -\frac{H_{j+\frac{1}{2}}(t) - H_{j-\frac{1}{2}}(t)}{\Delta x}; \tag{2.17}$$

here $H_{j\pm\frac{1}{2}}(t)$ are the numerical fluxes given by

$$H_{j+\frac{1}{2}}(t) := \frac{f(u^+_{j+\frac{1}{2}}(t)) + f(u^-_{j+\frac{1}{2}}(t))}{2} - \frac{a_{j+\frac{1}{2}}(t)}{2}\left[u^+_{j+\frac{1}{2}}(t) - u^-_{j+\frac{1}{2}}(t)\right]. \tag{2.18}$$

Once again, we emphasize that among its several advantages, the versatility of this semidiscrete formulation is the independence of the specific reconstruction, (2.3), and evolution algorithms which are utilized to recover the interface values $u^-_{j+\frac{1}{2}}$ and $u^+_{j+\frac{1}{2}}$ and to evolve the cell averages in (2.17). A description of our particular choices for these algorithms is provided in section 3.

2.2. Two-dimensional schemes. Starting with a general hyperbolic conservation law in two space dimensions,

$$u_t + f(u)_x + g(u)_z = 0, \tag{2.19}$$

we proceed as in section 2.1 and consider the sliding averages of u over the cells $I_{j,k} := [x_{j-1/2}, x_{j+1/2}] \times [z_{k-1/2}, z_{k+1/2}]$,

$$\bar{u}^n_{j,k} := \fint_{I_{j,k}} u(x,z,t^n)\, dx\, dz,$$

where Δx and Δz represent the space scales in the x- and the z-direction, respectively.

As in the one-dimensional case, we seek a semidiscrete formulation for the evolution of the cell averages of the conservation law (2.19). We begin by incorporating

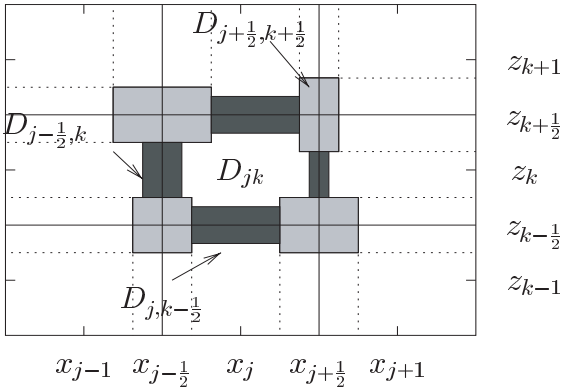

FIG. 2.2. *Floor plan for modified central differencing in two space dimensions.*

the information provided by the local speeds of propagation, which we approximate by

$$
\begin{aligned}
a^n_{j+\frac{1}{2},k} &:= \max\left\{\rho\left(\frac{\partial f}{\partial u}\left(u^W_{j+1,k}\right)\right), \rho\left(\frac{\partial f}{\partial u}\left(u^E_{j,k}\right)\right)\right\}, \quad b^n_{j,k+\frac{1}{2}}, \\
&:= \max\left\{\rho\left(\frac{\partial g}{\partial u}\left(u^S_{j,k+1}\right)\right), \rho\left(\frac{\partial g}{\partial u}\left(u^N_{j,k}\right)\right)\right\},
\end{aligned} \tag{2.20}
$$

where the cell interface values in the z- and x-directions,

$$
\begin{aligned}
u^N_{j,k} &:= p^n_{j,k}(x_j, z_{k+\frac{1}{2}}), \quad u^S_{j,k} := p^n_{j,k}(x_j, z_{k-\frac{1}{2}}), \\
u^E_{j,k} &:= p^n_{j,k}(x_{j+\frac{1}{2}}, z_k), \quad u^W_{j,k} := p^n_{j,k}(x_{j-\frac{1}{2}}, z_k),
\end{aligned} \tag{2.21}
$$

are calculated via a nonoscillatory piecewise polynomial reconstruction,

$$
R(x, z; \bar{u}^n) = \sum_{j,k} p^n_{j,k}(x, z)\mathbf{1}_{I_{j,k}}; \tag{2.22}
$$

the polynomials $\{p^n_{j,k}(x,z)\}$ are determined so that $R(x, z; \bar{u}^n)$ satisfies properties analogous to $\mathcal{P}_1$ – $\mathcal{P}_3$ above. This information allows us to separate between regions of smoothness, depicted as $D_{j,k}$ in Figure 2.2, and regions of nonsmoothness, depicted as the shaded regions. Nine sets of cell averages are calculated as follows:

- In the clear shaded regions, $D_{j\pm\frac{1}{2},k\pm\frac{1}{2}}$, the solution is not smooth in both directions; staggered evolution over the control volumes $D_{j\pm\frac{1}{2},k\pm\frac{1}{2}} \times [t^n, t^{n+1}]$ is used to obtain the new cell averages $\{\bar{w}^{n+1}_{j\pm\frac{1}{2},k\pm\frac{1}{2}}\}$,
- In the dark shaded regions, $D_{j\pm\frac{1}{2},k}$ and $D_{j,k\pm\frac{1}{2}}$, the solution is smooth only in one direction; staggered evolution is used along the nonsmooth interfaces to obtain, respectively, the cell averages $\{\bar{w}^{n+1}_{j\pm\frac{1}{2},k}\}$ and $\{\bar{w}^{n+1}_{j,k\pm\frac{1}{2}}\}$,
- To evolve the smooth part of the solution, we integrate the polynomial $p^n_{j,k}(x,z)$ and the corresponding fluxes over the nonrectangular control volume $D_{j,k} \times [t^n, t^{n+1}]$; these cell averages are denoted by $\{\bar{w}^{n+1}_{j,k}\}$.

This approach allows us to form a new polynomial, denoted $R(x, z; \bar{w}^{n+1})$, which is reconstructed from these smooth and nonsmooth portions of the solution, and to

reproject it back onto the original grid-cells,

$$\bar{u}_{j,k}^{n+1} = \fint_{I_{j,k}} R\,(x,z;\bar{w}^{n+1})\,dx\,dz. \tag{2.23}$$

The resulting nonstaggered fully discrete scheme admits a more versatile semidiscrete limit as $\Delta t \to 0$,

$$\frac{d}{dt}\bar{u}_{j,k}(t) = -\frac{H^x_{j+\frac{1}{2},k}(t) - H^x_{j-\frac{1}{2},k}(t)}{\Delta x} - \frac{H^z_{j,k+\frac{1}{2}}(t) - H^z_{j,k-\frac{1}{2}}(t)}{\Delta z}, \tag{2.24}$$

with numerical fluxes

$$\begin{aligned} H^x_{j+\frac{1}{2},k}(t) = {} & \frac{1}{12}\Big[f\left(u^{NW}_{j+1,k}(t)\right) + f\left(u^{NE}_{j,k}(t)\right) + 4\Big(f\left(u^{W}_{j+1,k}(t)\right) \\ & + f\left(u^{E}_{j,k}(t)\right)\Big) + f\left(u^{SW}_{j+1,k}(t)\right) + f\left(u^{SE}_{j,k}(t)\right)\Big] \\ & - \frac{a_{j+\frac{1}{2},k}(t)}{12}\Big(u^{NW}_{j+1,k}(t) - u^{NE}_{j,k}(t) + 4\Big(u^{W}_{j+1,k}(t) \\ & - u^{E}_{j,k}(t)\Big) + u^{SW}_{j+1,k}(t) - u^{SE}_{j,k}(t)\Big), \end{aligned} \tag{2.25}$$

$$\begin{aligned} H^z_{j,k+\frac{1}{2}}(t) = {} & \frac{1}{12}\Big[g\left(u^{SW}_{j,k+1}(t)\right) + g\left(u^{NW}_{j,k}(t)\right) + 4\Big(g\left(u^{S}_{j,k+1}(t)\right) \\ & + g\left(u^{N}_{j,k}(t)\right)\Big) + g\left(u^{SE}_{j,k+1}(t)\right) + g\left(u^{NE}_{j,k}(t)\right)\Big] \\ & - \frac{b_{j,k+\frac{1}{2}}(t)}{12}\Big(u^{SW}_{j,k+1}(t) - u^{NW}_{j,k}(t) + 4\Big(u^{S}_{j,k+1}(t) \\ & - u^{N}_{j,k}(t)\Big) + u^{SE}_{j,k+1}(t) - u^{NE}_{j,k}(t)\Big). \end{aligned} \tag{2.26}$$

This particular version of the numerical fluxes results from using Simpson's quadrature rule to approximate the integrals of the fluxes f and g along the cell boundaries $[z_{k-\frac{1}{2}}, z_{k+\frac{1}{2}}]$ and $[x_{j-\frac{1}{2}}, x_{j+\frac{1}{2}}]$, respectively, and it incorporates information from the *corner* interface values,

$$\begin{aligned} u^{NE}_{j,k} &:= \hat{p}^n_{j,k}(x_{j+\frac{1}{2}}, z_{k+\frac{1}{2}}), \quad u^{SW}_{j,k} := \hat{p}^n_{j,k}(x_{j-\frac{1}{2}}, z_{k-\frac{1}{2}}), \\ u^{SE}_{j,k} &:= \hat{p}^n_{j,k}(x_{j+\frac{1}{2}}, z_{k-\frac{1}{2}}), \quad u^{NW}_{j,k} := \hat{p}^n_{j,k}(x_{j-\frac{1}{2}}, z_{k+\frac{1}{2}}), \end{aligned} \tag{2.27}$$

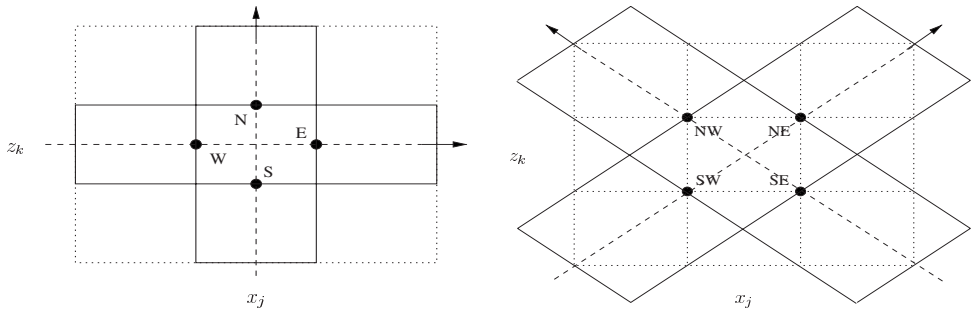

(a) (b)

FIG. 2.3. (a) *Reconstruction in x- and z-directions.* (b) *Diagonal axes for reconstruction.*

into the scheme. These corner values are recovered via the nonoscillatory reconstruction $\hat{R}(x,z;\bar{u}^n) = \sum \hat{p}^n_{j,k}(x,z)\cdot \mathbf{1}_{I_{j,k}}$, which may coincide with the original reconstruction, $R(x,z;\bar{u}^n)$, or, alternatively, interpolate the cell values along the diagonal directions shown in Figure 2.3(b) so as to prevent the onset of spurious oscillations along those axes.

3. Implementation of semidiscrete central schemes. The framework of the semidiscrete scheme described above entertains a wide range of options for the implementation of their two main ingredients: nonoscillatory reconstruction and evolution. In this section we provide some examples of nonoscillatory reconstructions and evolution routines that we implemented for computing the solutions of the system (1.1)–(1.4) presented in sections 4 and 5.

3.1. Third-order CWENO reconstruction. Our first choice for the reconstruction of the point values of u is the third-order CWENO polynomial reconstruction of Kurganov and Levy [12]. A piecewise quadratic polynomial that satisfies the essential properties $\mathcal{P}_1$, $\mathcal{P}_2$, and $\mathcal{P}_3$ above is formed as follows: in each cell $I_j = [x_{j-\frac{1}{2}}, x_{j+\frac{1}{2}}]$, the polynomials $\{p^n_j(x)\}$ in (2.3) are written as a convex combination of three polynomials $P_{\rm L}(x)$, $P_{\rm C}(x)$, and $P_{\rm R}(x)$,

$$p^n_j(x) = w_{\rm L}P_{\rm L}(x) + w_{\rm C}P_{\rm C}(x) + w_{\rm R}P_{\rm R}(x), \qquad \sum_{i\in\{{\rm L},{\rm C},{\rm R}\}} w_i = 1, \tag{3.1}$$

where the linear polynomials

$$P_{\rm L}(x) = \bar{u}^n_j + \frac{\bar{u}^n_j - \bar{u}^n_{j-1}}{\Delta x}(x - x_j) \quad \text{and} \quad P_{\rm R}(x) = \bar{u}^n_j + \frac{\bar{u}^n_{j+1} - \bar{u}^n_j}{\Delta x}(x - x_j), \tag{3.2}$$

conserve the pair of cell averages $\bar{u}^n_{j-1}$, $\bar{u}^n_j$ and $\bar{u}^n_j$, $\bar{u}^n_{j+1}$, respectively, and the parabola centered around x_j,

$$\begin{aligned} P_{\rm C}(x) = \bar{u}^n_j &- \frac{1}{12}(\bar{u}^n_{j-1} - 2\bar{u}^n_j + \bar{u}^n_{j+1}) \\ &+ \frac{\bar{u}^n_{j+1} - \bar{u}^n_{j-1}}{2\Delta x}(x - x_j) + \frac{\bar{u}^n_{j-1} - 2\bar{u}^n_j + \bar{u}^n_{j+1}}{\Delta x^2}(x - x_j)^2, \end{aligned} \tag{3.3}$$

is determined so as to satisfy

$$c_{\rm L}P_{\rm L}(x) + c_{\rm R}P_{\rm R}(x) + (1 - c_{\rm L} - c_{\rm R})P_{\rm C}(x) = u^n_j + u'_j(x - x_j) + \frac{1}{2}u''_j(x - x_j)^2,$$

where u^n_j, u'_j, and u''_j approximate the point values $u(x_j,t^n)$, $u_x(x_j,t^n)$, and $u_{xx}(x_j,t^n)$ given respectively by

$$\begin{aligned} u^n_j &:= \bar{u}^n_j - \frac{1}{24}(\bar{u}^n_{j-1} - 2\bar{u}^n_j + \bar{u}^n_{j+1}), \\ u'_j &:= \frac{\bar{u}^n_{j+1} - \bar{u}^n_{j-1}}{2\Delta x}, \quad \text{and} \quad u''_j := \frac{\bar{u}^n_{j-1} - 2\bar{u}^n_j + \bar{u}^n_{j+1}}{\Delta x^2}. \end{aligned} \tag{3.4}$$

We guarantee the conservation of the cell averages $\bar{u}^n_{j-1}$, $\bar{u}^n_j$, and $\bar{u}^n_{j+1}$ by any symmetric choice of the weights c_i (e.g., $c_{\rm L} = c_{\rm R} = 1/4$, $c_{\rm C} = 1/2$) and the accuracy property, $\mathcal{P}_2$, in smooth regions [17],

$$p^n_j(x) = u(x,t^n) + \mathcal{O}((\Delta x)^3), \quad x \in [x_{j-\frac{1}{2}}, x_{j+\frac{1}{2}}].$$

Property $\mathcal{P}_3$—the nonoscillatory behavior of $\{p_j^n(x)\}$ is attained with the nonlinear weights

$$w_i = \frac{\alpha_i}{\sum_m \alpha_m} \quad \text{with} \quad \alpha_i = \frac{c_i}{(\epsilon + IS_i)^2}, \quad i, m \in \{\text{L}, \text{C}, \text{R}\}, \tag{3.5}$$

where $\epsilon \ll 1$ prevents the denominator from vanishing (for the calculations in sections 4 and 5 we choose $\epsilon = 10^{-6}$), and the smoothness indicators, IS_i, provide a local measure of the derivatives of $P_i(x)$,

$$IS_i = \sum_{l=1}^{2} \int_{I_j} (\Delta x)^{2l-1} (P_i^{(l)}(x))^2 dx, \quad i \in \{\text{L}, \text{C}, \text{R}\}, \tag{3.6}$$

switching automatically to the second-order reconstructions P_{L} and P_{R} in the presence of steep gradients and avoiding the onset of spurious oscillations [9, 12, 17]. In this case, they read

$$\begin{aligned} IS_{\text{L}} &= (\bar{u}_j^n - \bar{u}_{j-1}^n)^2, \qquad IS_{\text{R}} = (\bar{u}_{j+1}^n - \bar{u}_j^n)^2, \\ IS_{\text{C}} &= \frac{13}{3}(\bar{u}_{j+1}^n - 2\bar{u}_j^n + \bar{u}_{j-1}^n)^2 + \frac{1}{4}(\bar{u}_{j+1}^n - \bar{u}_{j-1}^n)^2. \end{aligned} \tag{3.7}$$

Remarks.

1. For this particular reconstruction, the one-dimensional interface values, $u^-_{j+\frac{1}{2}}(t)$ and $u^+_{j+\frac{1}{2}}(t)$, required in the numerical flux (2.18) take the explicit form

$$\begin{aligned} u^-_{j+\frac{1}{2}}(t^n) := p_j^n(x_{j+\frac{1}{2}}) &= \frac{1}{2} w_{\text{L}}(3\bar{u}_j^n - \bar{u}_{j-1}^n) \\ &\quad + \frac{1}{12} w_{\text{C}}(-5\bar{u}_{j+1}^n + 8\bar{u}_j^n - \bar{u}_{j-1}^n) + \frac{1}{2} w_{\text{R}}(\bar{u}_{j+1}^n + \bar{u}_j^n), \\ u^+_{j+\frac{1}{2}}(t^n) := p_{j+1}^n(x_{j+\frac{1}{2}}) &= \frac{1}{2} w_{\text{L}}(\bar{u}_{j+1}^n + \bar{u}_j^n) \\ &\quad + \frac{1}{12} w_{\text{C}}(-\bar{u}_{j+2}^n + 8\bar{u}_{j+1}^n - 5\bar{u}_j^n) + \frac{1}{2} w_{\text{R}}(-\bar{u}_{j+2}^n + 3\bar{u}_{j+1}^n). \end{aligned}$$

2. In the case of systems of equations, the choice of these smoothness indicators is, indeed, nontrivial. The different conserved quantities involved in any particular system (density, momentum, etc.) may very well develop discontinuities at different points throughout the solution domain that do not affect every other quantity in the system. Hence, choosing the smoothness indicators individually for each quantity may cause the scheme to use different stencils for different quantities during the same evolution step. This can be avoided by either using *global* smoothness indicators, e.g., an (norm-scaled) average of the individual ones, or by identifying those that are physically relevant, such as, e.g., the density near a contact discontinuity. (See section 4 for our particular choices in the one-dimensional case and [16] for an in-depth discussion about the selection of smoothness indicators for systems of equations.)

In two and higher space dimensions, a possibility for calculating the interface values in (2.21) and (2.27) in a rather straightforward way is to apply this one-dimensional third-order reconstruction *dimension by dimension* in the x- and z-directions (Figure 2.3(a)) and, if so desired, in the two diagonal directions of the coordinate frame displayed in Figure 2.3(b). In two dimensions, however, we note that the constant

term in the *central* parabola, (3.3), requires an additional correction (in the transverse direction of the reconstruction) in order to guarantee third-order accuracy when the point value $u(x_j, z_k, t^n)$ is recovered from the neighboring cell averages,

$$u(x_j, z_k, t^n) = \bar{u}^n_{j,k} - \frac{1}{12}(\bar{u}^n_{j-1,k} - 2\bar{u}^n_{j,k} + \bar{u}^n_{j+1,k}) - \frac{1}{12}(\bar{u}^n_{j,k-1} - 2\bar{u}^n_{j,k} + \bar{u}^n_{j,k+1}) + \mathcal{O}((\max\{\Delta x, \Delta z\})^3).$$

That is, along the line $z = z_k$, the reconstruction in the x-direction is carried out using the linear polynomials $P_{\rm L}(x, z_k)$ and $P_{\rm R}(x, z_k)$ as in (3.2), and the parabola $P_{\rm C}(x, z_k)$, given by

$$P_{\rm C}(x, z_k) = \bar{u}^n_{j,k} - \frac{1}{12}(\bar{u}^n_{j-1,k} - 2\bar{u}^n_{j,k} + \bar{u}^n_{j+1,k}) - \frac{1}{12}(\bar{u}^n_{j,k-1} - 2\bar{u}^n_{j,k} + \bar{u}^n_{j,k+1}) + \frac{\bar{u}^n_{j+1,k} - \bar{u}^n_{j-1,k}}{2\Delta x}(x - x_j) + \frac{\bar{u}^n_{j-1,k} - 2\bar{u}^n_j + \bar{u}^n_{j+1,k}}{\Delta x^2}(x - x_j)^2. \tag{3.8}$$

The same reconstruction is carried out in the z-direction, holding $x = x_j$ fixed. And, should one choose to implement the reconstruction along the diagonal directions, the corresponding polynomials are given by (consult [13] for additional details)

$$\hat{p}^n_{j,k}(x, z) = \hat{w}_{\rm L}\hat{P}_{\rm L}(x, z) + \hat{w}_{\rm C}\hat{P}_{\rm C}(x, z) + \hat{w}_{\rm R}\hat{P}_{\rm R}(x, z) \tag{3.9}$$

with

$$\hat{P}_{\rm L}(x, z) = \bar{u}^n_{j,k} + \frac{\bar{u}^n_{j,k} - \bar{u}^n_{j-1,k-1}}{\Delta}\left(\frac{\Delta}{2\Delta z}(z - z_k) + \frac{\Delta}{2\Delta x}(x - x_j)\right),$$

$$\hat{P}_{\rm C}(x, z) = \bar{u}^n_{j,k} - \frac{1}{12}(\bar{u}^n_{j+1,k+1} - 2\bar{u}^n_{j,k} + \bar{u}^n_{j-1,k-1}) - \frac{1}{12}(\bar{u}^n_{j-1,k+1} - 2\bar{u}^n_{j,k} + \bar{u}^n_{j+1,k-1}) + \frac{\bar{u}^n_{j+1,k+1} - \bar{u}^n_{j-1,k-1}}{2\Delta}\left(\frac{\Delta}{2\Delta z}(z - z_k) + \frac{\Delta}{2\Delta x}(x - x_j)\right) + \frac{\bar{u}^n_{j+1,k+1} - 2\bar{u}^n_{j,k} + \bar{u}^n_{j-1,k-1}}{\Delta^2}\left(\frac{\Delta}{2\Delta z}(z - z_k) + \frac{\Delta}{2\Delta x}(x - x_j)\right)^2,$$

$$\hat{P}_{\rm R}(x, z) = \bar{u}^n_{j,k} + \frac{\bar{u}^n_{j+1,k+1} - \bar{u}^n_{j,k}}{\Delta}\left(\frac{\Delta}{2\Delta z}(z - z_k) + \frac{\Delta}{2\Delta x}(x - x_j)\right) \tag{3.10}$$

along the SW–NE axis and

$$\hat{P}_{\rm L}(x, z) = \bar{u}^n_{j,k} + \frac{\bar{u}^n_{j,k} - \bar{u}^n_{j+1,k-1}}{\Delta}\left(\frac{\Delta}{2\Delta z}(z - z_k) - \frac{\Delta}{2\Delta x}(x - x_j)\right),$$

$$\hat{P}_{\rm C}(x, z) = \bar{u}^n_{j,k} - \frac{1}{12}(\bar{u}^n_{j+1,k+1} - 2\bar{u}^n_{j,k} + \bar{u}^n_{j-1,k-1}) - \frac{1}{12}(\bar{u}^n_{j-1,k+1} - 2\bar{u}^n_{j,k} + \bar{u}^n_{j+1,k-1}) + \frac{\bar{u}^n_{j-1,k+1} - \bar{u}^n_{j+1,k-1}}{2\Delta}\left(\frac{\Delta}{2\Delta z}(z - z_k) - \frac{\Delta}{2\Delta x}(x - x_j)\right) + \frac{\bar{u}^n_{j-1,k+1} - 2\bar{u}^n_{j,k} + \bar{u}^n_{j+1,k-1}}{\Delta^2}\left(\frac{\Delta}{2\Delta z}(z - z_k) - \frac{\Delta}{2\Delta x}(x - x_j)\right)^2,$$

$$\hat{P}_{\rm R}(x, z) = \bar{u}^n_{j,k} + \frac{\bar{u}^n_{j+1,k+1} - \bar{u}^n_{j,k}}{\Delta}\left(\frac{\Delta}{2\Delta z}(z - z_k) - \frac{\Delta}{2\Delta x}(x - x_j)\right) \tag{3.11}$$

along the SE–NW axis, where $\Delta = \sqrt{(\Delta x)^2 + (\Delta z)^2}$. The nonlinear weights, $\hat{w}_i$, are also calculated direction by direction according to the one-dimensional recipe (3.5) with the smoothness indicators given by the *norm-scaled* average of the componentwise indicators, $IS_i^{(m)}$, calculated as in (3.7),

$$IS_i = \frac{1}{d}\sum_{m=1}^{d} \frac{1}{\|u^{(m)}\|_2 + \epsilon}\, IS_i^{(m)}, \quad i \in \{\text{L}, \text{C}, \text{R}\}, \tag{3.12}$$

where $u^{(m)}$ stands for the mth component of u, and $\|u^{(m)}\|_2^2 = \sum_{j,k} |u_{j,k}^{(m)}|^2 \Delta x \Delta z$ represents its ℓ_2 norm over the discretized solution domain.

3.2. CWENO fourth-order reconstruction. In section 5 we demonstrate the versatility of the central semidiscrete scheme (2.24)–(2.26) by implementing the dimension-by-dimension third-order reconstruction described above and the *genuinely multidimensional* fourth-order CWENO reconstruction of Levy, Puppo, and Russo [18] and Balbás [1] that recovers the interface point values in (2.21) and (2.27) via a biquadratic polynomial interpolant satisfying the desired conservation, accuracy, and nonoscillatory properties in two-space dimensions. Following is an outline of this fourth-order reconstruction, originally developed by Levy and others within the central, fully discrete, staggered framework. In each cell $I_{j,k}$, the piecewise polynomial interpolants in (2.22), $p_{j,k}^n(x,z)$, are written as a convex combination of nine biquadratic polynomials, $P_{j+p,k+q}(x,z)$, that conserve the cell averages $\{\bar{u}_{j+p,k+q}^n\}_{p,q=-1}^{1}$ and approximate the point values of $u(x,z,t^n)$ within fourth-order accuracy,

$$p_{j,k}^n(x,z) = \sum_{p,q=-1}^{1} w_{j,k}^{p,q} P_{j+p,k+q}(x,z), \qquad \sum_{p,q=-1}^{1} w_{j,k}^{p,q} = 1, \quad w_{j,k}^{p,q} \geq 0, \tag{3.13}$$

where the polynomials $P_{j,k}(x,z)$ have the form (omitting, for simplicity, the j and k indices in the coefficients $\{b_m\}$),

$$\begin{aligned} P_{j,k}^n(x,z) = {} & b_0 + b_1(x - x_j) + b_2(z - z_k) + b_3(x - x_j)(z - z_k) \\ & + b_4(x - x_j)^2 + b_5(z - z_k)^2 + b_6(x - x_j)^2(z - z_k) \\ & + b_7(x - x_j)(z - z_k)^2 + b_8(x - x_j)^2(z - z_k)^2. \end{aligned} \tag{3.14}$$

The nine conservation constraints,

$$\int_{x_{j-\frac{1}{2}}+p\Delta x}^{x_{j+\frac{1}{2}}+p\Delta x} \int_{z_{k-\frac{1}{2}}+q\Delta z}^{z_{k+\frac{1}{2}}+q\Delta z} P_{j,k}(x,z)\, dz\, dx = \bar{u}_{j+p,k+q}^n, \quad p,q = -1,0,1, \tag{3.15}$$

uniquely determine the nine coefficients $\{b_m\}$,

$$\begin{aligned} b_0 &= \bar{u}^n - \frac{\Delta x^2}{24}\hat{u}_{xx} - \frac{\Delta z^2}{24}\hat{u}_{zz} + \frac{\Delta x^2 \Delta z^2}{24^2}\hat{u}_{xxzz}, \\ b_1 &= \hat{u}_x - \frac{\Delta z^2}{24}\hat{u}_{xzz}, & b_2 &= \hat{u}_z - \frac{\Delta x^2}{24}\hat{u}_{xxz}, \\ b_3 &= \hat{u}_{xz}, & b_4 &= \frac{1}{2}\hat{u}_{xx} - \frac{\Delta z^2}{48}\hat{u}_{xxzz}, \\ b_5 &= \frac{1}{2}\hat{u}_{zz} - \frac{\Delta x^2}{48}\hat{u}_{xxzz}, & b_6 &= \frac{1}{2}\hat{u}_{xxz}, \\ b_7 &= \frac{1}{2}\hat{u}_{xzz}, & b_8 &= \frac{1}{4}\hat{u}_{xxzz}, \end{aligned}$$

where the divided differences

$$\hat{u}_{x_{j,k}} = \frac{\bar{u}^n_{j+1,k} - \bar{u}^n_{j-1,k}}{2\Delta x}, \qquad \hat{u}_{z_{j,k}} = \frac{\bar{u}^n_{j,k+1} - \bar{u}^n_{j,k-1}}{2\Delta z},$$
$$\hat{u}_{xx_{j,k}} = \frac{\bar{u}^n_{j+1,k} - 2\bar{u}^n_{j,k} + \bar{u}^n_{j-1,k}}{\Delta x^2}, \qquad \hat{u}_{zz_{j,k}} = \frac{\bar{u}^n_{j,k+1} - 2\bar{u}^n_{j,k} + \bar{u}^n_{j,k-1}}{\Delta z^2},$$
$$\hat{u}_{xz_{j,k}} = \frac{\bar{u}^n_{j+1,k+1} - \bar{u}^n_{j+1,k-1} - \bar{u}^n_{j-1,k+1} + \bar{u}^n_{j-1,k-1}}{4\Delta x \Delta z},$$
$$\hat{u}_{xxz_{j,k}} = \frac{(\bar{u}^n_{j+1,k+1} - 2\bar{u}^n_{j,k+1} + \bar{u}^n_{j-1,k+1}) - (\bar{u}^n_{j+1,k-1} - 2\bar{u}^n_{j,k-1} + \bar{u}^n_{j-1,k-1})}{2\Delta x^2 \Delta z},$$
$$\hat{u}_{xzz_{j,k}} = \frac{(\bar{u}^n_{j+1,k+1} - 2\bar{u}^n_{j+1,k} + \bar{u}^n_{j+1,k-1}) - (\bar{u}^n_{j-1,k+1} - 2\bar{u}^n_{j-1,k} + \bar{u}^n_{j-1,k-1})}{2\Delta x \Delta z^2},$$
$$\hat{u}_{xxzz_{j,k}} = \frac{1}{\Delta x^2 \Delta z^2}\big[(\bar{u}^n_{j+1,k+1} - 2\bar{u}^n_{j+1,k} + \bar{u}^n_{j+1,k-1}) - 2(\bar{u}^n_{j,k+1} - 2\bar{u}^n_{j,k} + \bar{u}^n_{j,k-1}) + (\bar{u}^n_{j-1,k+1} - 2\bar{u}^n_{j-1,k} + \bar{u}^n_{j-1,k-1})\big]$$

serve to approximate the values of u and its partial derivatives at the points (x_j, z_k) within the fourth-order accuracy constraints of the method.

As in the third-order reconstruction, the nonlinear weights in (3.13), $w^{p,q}_{l,k}$, are computed so as to provide maximum accuracy in smooth regions and prevent oscillations in the nonsmooth regions by eliminating the contribution of polynomials with steep gradients across the cell interfaces. For each cell nine weights are calculated,

$$w^{p,q}_{j,k} = \frac{\alpha^{p,q}_{j,k}}{\sum_{m,n} \alpha^{m,n}_{j,k}} \quad \text{with} \quad \alpha^{p,q}_{j,k} = \frac{c^{p,q}_{j,k}}{(\epsilon + IS^{p,q}_{j,k})^2}, \quad m,n,p,q = -1,0,1, \tag{3.16}$$

and the linear coefficients, $c^{p,q}_{j,k}$, chosen so that symmetry guarantees fourth-order accuracy,

$$c^{0,0}_{j,k} = \frac{1}{2} \qquad \text{and} \qquad c^{p,q}_{j,k} = \frac{1}{16} \quad \forall\ p,q \neq 0;$$

convexity, $\sum^{1}_{p,q=-1} c^{p,q}_{j,k} = 1$, $c^{p,q}_{j,k} \geq 0$, guarantees conservation.

Global smoothness indicators are chosen according to (3.12). Unlike the third-order reconstruction where the exact calculation of the individual smoothness indicators is trivial and renders simple formulas, i.e., (3.7), in this fourth-order case, the exact calculation of the local L^2-norm of the partial derivatives of the polynomials $P^{p,q}_{j,k}$ is impractical. Instead, a Gaussian quadrature formula is used to approximate the integrals

$$IS^{p,q}_{j,k} = \int_{I_{j,k}} (|\partial_x P_{j+p,k+q}|^2 + |\partial_z P_{j+p,k+q}|^2 + (\Delta x)^2 |\partial_{xx} P_{j+p,k+q}|^2 + (\Delta z)^2 |\partial_{zz} P_{j+p,k+q}|^2)\, dx\, dz.$$

This approach still serves the purpose of automatically detecting and redirecting the numerical stencils in the direction of smoothness, thus preventing the onset of oscillations, [18].

3.3. Time evolution: Strong stability-preserving Runge–Kutta solvers. With the interface values (2.16), (2.21), and (2.27) computed with either of the above

CWENO reconstructions, we denote, for any grid function $w = \{w_j(t)\}$, the numerical fluxes on the right of (2.17) and (2.24) by

$$C[w(t)] = -\frac{H_{j+\frac{1}{2}}(w(t)) - H_{j-\frac{1}{2}}(w(t))}{\Delta x} \tag{3.17}$$

and

$$C[w(t)] = -\frac{H^x_{j+\frac{1}{2},k}(w(t)) - H^x_{j-\frac{1}{2},k}(w(t))}{\Delta x} - \frac{H^z_{j,k+\frac{1}{2}}(w(t)) - H^z_{j,k-\frac{1}{2}}(w(t))}{\Delta z}, \tag{3.18}$$

respectively, and evolve the solution $u^{(0)} := \bar{u}^n_j$ from t^n, to t^{n+1} with an appropriate ODE solver. For the numerical calculations reported in sections 4 and 5, we choose the strong stability-preserving (SSP) Runge–Kutta discretizations [23, 5]. In particular, for the third-order results, we employ

$$\begin{aligned} u^{(1)} &= u^{(0)} + \Delta t C[u^{(0)}], \\ u^{(2)} &= u^{(1)} + \frac{\Delta t}{4}(-3C[u^{(0)}] + C[u^{(1)}]), \\ u^{n+1} := u^{(3)} &= u^{(2)} + \frac{\Delta t}{12}(-C[u^{(0)}] - C[u^{(1)}] + 8\ C[u^{(2)}]), \end{aligned} \tag{3.19}$$

and for the fourth-order results of section 5.3,

$$\begin{aligned} u^{(1)} &= u^{(0)} + \frac{\Delta t}{2} C[u^{(0)}], \\ u^{(2)} &= u^{(1)} + \frac{\Delta t}{2}(-C[u^{(0)}] + C[u^{(1)}]), \\ u^{(3)} &= u^{(2)} + \frac{\Delta t}{2}(-C[u^{(1)}] + 2\ C[u^{(2)}]), \\ u^{n+1} := u^{(4)} &= u^{(3)} + \frac{\Delta t}{6}(C[u^{(0)}] + 2C[u^{(1)}] - 4C[u^{(2)}] + C[u^{(3)}]) \end{aligned} \tag{3.20}$$

is used to evolve the values reconstructed via the fourth-order CWENO interpolation algorithm of Levy and others of section 3.2.

4. One-dimensional numerical results. In one space dimension, equations (1.1)–(1.4) admit the conservative form (2.1) with

$$u = (\rho, \rho v_x, \rho v_y, \rho v_z, B_y, B_z, e)^\top, \tag{4.1}$$

$$\begin{aligned} f(u) = (&\rho v_x, \rho v_x^2 + p^* - B_x^2, \rho v_x v_y - B_x B_y, \rho v_x v_z - B_x B_z, B_y v_x - B_x v_y, \\ &B_z v_x - B_x v_z, (e + p^*) v_x - B_x (B_x v_x + B_y v_y + B_z v_z))^\top, \end{aligned} \tag{4.2}$$

where $p^* = p + \frac{1}{2}B^2$ stands for the total pressure (static plus magnetic).

In this section we present numerical simulations of the one-dimensional MHD equations, (2.1)–(4.2). The results were obtained using the semidiscrete central scheme (2.17)–(2.18) with the pointvalues $u^+_{j+\frac{1}{2}}(t)$ and $u^-_{j+\frac{1}{2}}(t)$, (2.16), computed via the CWENO third-order reconstruction of section 3.1, and evolved according to Shu's third-order SSP Runge–Kutta scheme as outlined in section 3.3. The schemes are implemented for computing the approximate solution of two coplanar shock tube MHD models described by Brio and Wu in [3]. We use a uniform grid in the space

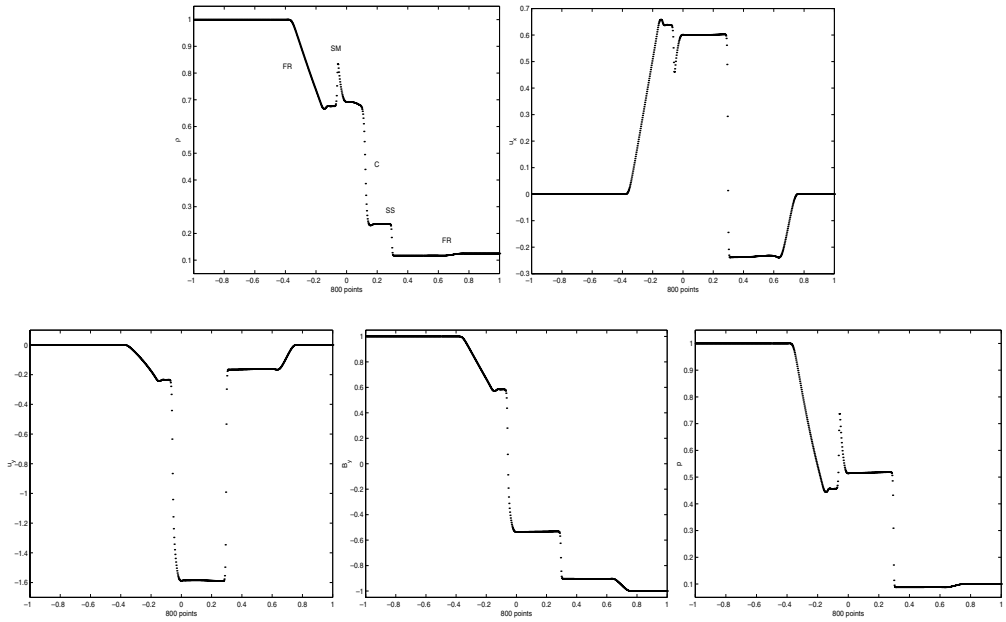

FIG. 4.1. *Results of Brio–Wu shock tube problem at* $t = 0.2$ *computed with* 800 *grid points using third-order CWENO reconstruction,* (3.1)*, and Shu's SSP Runge–Kutta solver,* (3.19).

discretization, and in both cases we choose the time step dynamically with CFL restriction

$$\Delta t = \frac{0.9\ \Delta x}{\max_k |a_k(u)|}, \tag{4.3}$$

where $\{a_k(u)\}_k$ are the eigenvalues of the Jacobian matrix of $f(u)$.

4.1. Brio–Wu shock tube problem. The first one-dimensional Riemann problem we consider consists of a shock tube with two initial equilibrium states, u_l and u_r, given by

$$(\rho, v_x, v_y, v_z, B_y, B_z, p)^\top = \begin{cases} (1.0, 0, 0, 0, 1.0, 0, 1.0)^\top & \text{for } x < 0, \\ (0.125, 0, 0, 0, -1.0, 0, 0.1)^\top & \text{for } x > 0, \end{cases} \tag{4.4}$$

and complemented with the constant values of $B_x \equiv 0.75$ and $\gamma = 2$. The problem is solved for $x \in [-1, 1]$ with 800 grid points, and numerical results are presented at $t = 0.2$. Figure 4.1 shows the density, the x- and y-velocity components, the y-magnetic field, and pressure profiles. The hydrodynamical data of this problem is the same as that in Sod's shock tube problem of gas dynamics. The variety of MHD waves, however, poses a considerable challenge for high resolution such as the *black-box* central schemes described in this paper. The solution of this problem consists of a left-moving fast rarefaction wave (FR), a slow compound wave (SM) which results from an intermediate shock that changes B_y from 0.58 to -0.31 and a slow rarefaction that changes B_y from -0.31 -0.53, a contact discontinuity (C), a right-moving slow shock (SS), and a right-moving fast rarefaction wave (FR). Note that the solution to this problem is not unique if B_z and v_z are not identically zero. The results in Figure 4.1 are in agreement with those previously reported in [2] and are comparable with

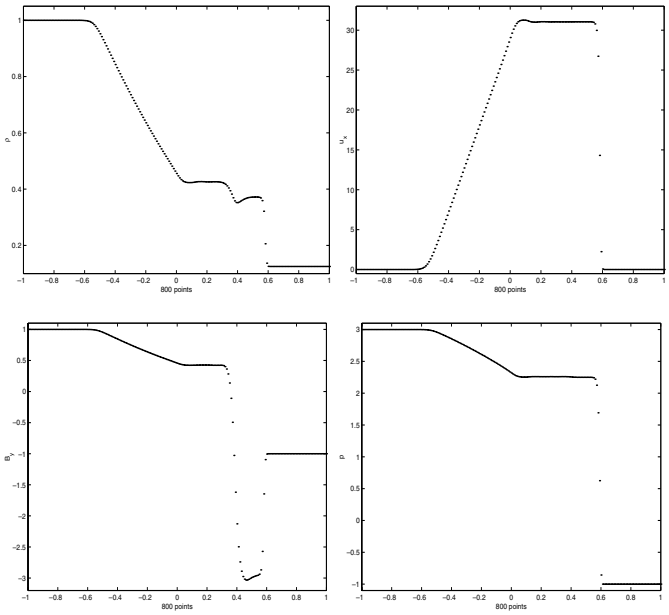

FIG. 4.2. *Results of Brio–Wu high Mach problem at* $t = 0.012$ *computed with* 200 *grid points using third-order CWENO reconstruction,* (3.1)*, and Shu's SSP Runge–Kutta solver,* (3.19).

the second-order upwind computations of Brio and Wu in [3] and with the fifth-order WENO computations presented by Jiang and Wu in [11]. In fact, the present results show a better control of the oscillations that typically appear at the trailing edge of the right-moving fast rarefaction wave when high-resolution schemes are employed. This better control is due to our choice of smoothness indicators. Our various numerical experiments show that in the absence of characteristic information, the average of the smoothness indicators of the density, ρ, and transverse magnetic field, B_y, scaled by their ℓ_2 norm, is the best combination for selecting a single stencil for reconstruction and evolution of all the conserved quantities in the system. Our numerical results confirm the ability of central schemes, whether in their fully discrete or semidiscrete formulations, to capture the main features of the discontinuous MHD solutions, while avoiding any characteristic information other than an estimate of the maximal speed of propagation, $\max_k |a_k(u)|$.

4.2. Brio–Wu high Mach shock tube problem. The following shock tube model proposed by Brio and Wu in [3] is commonly used to check the robustness of the numerical schemes for high Mach number problems. The initial equilibrium states, u_l and u_r, are given by

$$(\rho, v_x, v_y, v_z, B_y, B_z, p)^\top = \begin{cases} (1.0, 0, 0, 0, 1.0, 0, 1000)^\top & \text{for } x < 0, \\ (0.125, 0, 0, 0, -1.0, 0, 0.1)^\top & \text{for } x > 0 \end{cases} \tag{4.5}$$

and complemented with the values of $B_x \equiv 0$ and $\gamma = 2$. The Mach number of the right-moving shock wave is 15.5. If the plasma pressure is replaced by the sum of the static and magnetic pressures, denoted by p^* above, this model becomes a standard hydrodynamical Riemann problem. The solution is presented at $t = .012$, $x \in [-1, 1]$, with 200 grid points and with CFL number 0.9; consult (4.3).

The solution of this second Riemann problem consists of a left-moving fast rarefaction wave (FR), followed by a tangential discontinuity (TD), and a right-moving fast shock (FS) with Mach number 15.5. Across the tangential discontinuity, the density, the magnetic field, and the pressure can change, but both the fluid velocity and the total pressure, $p + \frac{B^2}{2}$, are continuous.

As in the previous problem, our results in Figure 4.2 are comparable to those reported in [2], [3], and [11] with second-order central and second- and fifth-order upwind schemes and demonstrate the robustness of the schemes described in section 2.

5. Two-dimensional numerical results. In two space dimensions, equations (1.1)–(1.4) admit the conservative form (2.19) with

$$u = (\rho, \rho v_x, \rho v_y, \rho v_z, B_x, B_y, B_z, e)^\top, \tag{5.1}$$

$$f(u) = (\rho v_x, \rho v_x^2 + p^* - B_x^2, \rho v_x v_y - B_x B_y, \rho v_x v_z - B_x B_z, 0, B_y v_x - B_x v_y, B_z v_x - B_x v_z, (e + p^*)v_x - B_x(B_x v_x + B_y v_y + B_z v_z))^\top, \tag{5.2}$$

$$g(u) = (\rho v_z, \rho v_z v_x - B_z B_x, \rho v_z v_y - B_z B_y, \rho v_z^2 + p^* - B_z^2, B_x v_z - B_z v_x, B_y v_z - B_z v_y, 0, (e + p^*)v_z - B_z(B_x v_x + B_y v_y + B_z v_z))^\top. \tag{5.3}$$

In this section we present the solution of four prototype problems for two-dimensional MHD equations. We begin testing our two-dimensional numerical schemes by solving the one-dimensional Brio–Wu shock tube problem described in section 4.1 on a two-dimensional domain with the flow rotated 45°. For the second problem—the Kelvin–Helmholtz instability with transverse magnetic field configuration—we consider two different sets of boundary conditions in the x-direction: periodic in the first case and a free outflow boundary in the second convective setup. The third problem was introduced by Orszag and Tang in [21] as a simple model to study MHD turbulence. The last problem that we present simulates the interaction between a strong shock and a high-density cloud. These four problems appear extensively in the literature as they have become—in the absence of a rigorous stability condition for numerical schemes for MHD equations—standard tests to validate numerical algorithms. In all cases, the time scale Δt is determined dynamically according to the CFL restriction

$$\Delta t = \frac{c}{\sqrt{(\max_k |a_k(u)|/\Delta x)^2 + (\max_k |b_k(u)|/\Delta z)^2}}, \tag{5.4}$$

where $c < 1$ is a positive constant and $\{a_k(u)\}_k$ and $\{b_k(u)\}_k$ represent the eigenvalues of the Jacobian matrices of $f(u)$ and $g(u)$, respectively.

It should be emphasized that the results presented below were obtained with the original formulation of semidiscrete central schemes in section 2, namely, they were implemented "as is," *without* any enforcement of the solenoidal constraint (1.5). The $\nabla \cdot \mathbf{B} = 0$-constraint was *automatically* preserved to machine round-off error. In fact, the same test problems displayed below were first solved using the (global) projection method as a way to enforce the $\nabla \cdot \mathbf{B} = 0$-constraint. We observed that the divergence-free results displayed below avoid undesirable effects such as loss of conservation and monotonicity, often induced by global projection solvers.

5.1. Brio–Wu rotated flow. The initial conditions described by (4.4) are extended to the two-dimensional domain $[-1, 1] \times [-1, 1]$ and rotated 45° so that the fluid does not flow in the direction of the grid axis. Our results are displayed in

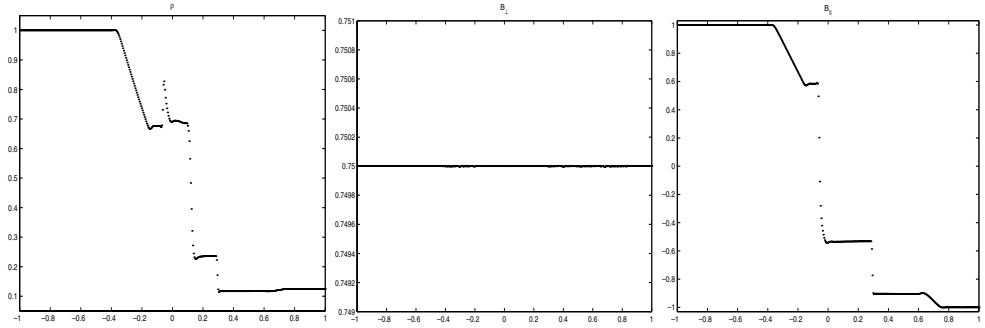

FIG. 5.1. *Results of rotated Brio–Wu shock tube problem at* $t = 0.2$ *computed over a* 600×600 *mesh using third-order dimension-by-dimension CWENO reconstruction,* (3.1)*, and Shu's SSP Runge–Kutta solver,* (3.19)*. From left to right: density, transverse, and parallel components of magnetic field (bottom)*

Figure 5.1, and they confirm the ability of central schemes to simulate discontinuous flows independently of the mesh orientation.

We observe that the small deviations from the constant value of the transverse component of the magnetic that can be observed in Figure 5.1 are well within the order of the scheme, and the numerical value of $\nabla \cdot \mathbf{B}$ is in the order of 10^{-13}.

5.2. Transverse Kelvin–Helmholtz instability. The Kelvin–Helmholtz instability arises when two superposed fluids flow one over the other with a relative velocity. It models, for example, the important mechanism for the momentum transfer at the Earth's magnetopause boundary, which separates the solar wind from the Earth's magnetosphere [11]. We approximate the solution of the two-dimensional periodic and convective models with transverse magnetic field configuration with the semidiscrete scheme of Kurganov and Tadmor, (2.24)–(2.26), implemented along with the reconstruction of section 3.1 and the SSP Runge–Kutta solver (3.19). In both cases, the governing equations are (5.1)–(5.3) are subject to initial conditions

$$(\rho, v_x, v_y, v_z, B_x, B_y, B_z, p)^\top = (1.0, v_{x0} + \tilde{v}_{x0}, 0, 0, 0, 1.0, 0, 0.5)^\top, \tag{5.5}$$

where

$$v_{x0} = \frac{v_0}{2} \tanh\left(\frac{z}{a}\right) \quad \text{and} \tag{5.6}$$

$$\tilde{v}_{x0} = \begin{cases} -\tilde{v}_0 \sin\left(\frac{2\pi x}{\lambda}\right) \frac{1}{1+z^2} & \text{if } -\frac{\lambda}{2} < x < \frac{\lambda}{2} \\ 0 & \text{otherwise} \end{cases}, \tag{5.7}$$

with $v_0 = 2$, $\tilde{v}_0 = -0.008$, $\lambda = 5\pi$, and $a = 1$. Also, the grids are stretched in the z-direction with a Roberts transformation [11],

$$z \leftarrow \frac{H \sinh(\tau z/2H)}{\sinh(\tau/2)}, \quad \tau = 6, \tag{5.8}$$

which renders a denser grid near $z = 0$, where the effect of the small initial perturbation $\tilde{v}_{x0}$ is more noticeable, and a coarser grid near $z = \pm H$, where little action takes place. The time step, Δt, is determined according to (5.4) with $c = 0.9$.

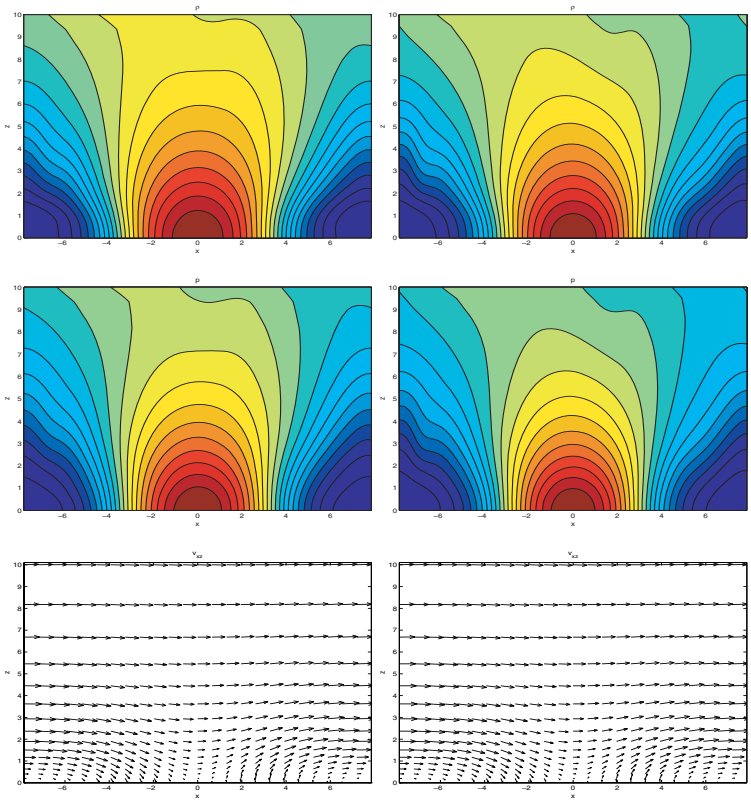

FIG. 5.2. *Results of transverse Kelvin–Helmholtz instability with periodic x-boundary conditions computed with third-order scheme. Left column uses 72×45 points and right column uses 96×60 grids, respectively. There are 20 contours for density and pressure, where darker colors indicate higher values. The density ranges from 0.79 to 1.2, the pressure ranges from 0.32 to 0.71, and the maximum value for the velocity is 1.25.*

In the periodic case, the computational domain is $[-\frac{L}{2}, \frac{L}{2}] \times [0, H]$, with $L = 5\pi$ and $H = 10$. The free outflow condition is applied at the top boundary, $z = H$, and the bottom boundary values are recovered by symmetry, since ρ, p, and B_y are symmetric, and v_x and v_z are antisymmetric under the transformation $(x, z) \to (-x, -z)$. In Figure 5.2, we present solutions at $t = 144$ with 72×45 and 96×60 grid points. The resolution and accuracy of our results are comparable to those reported in [2] obtained over two grids of sizes 96×96 and a 192×192, respectively, with the second-order staggered central scheme of Jiang and Tadmor; the gas kinetic scheme of Tang and Xu, [26], using a 200×200 uniform grid; and to those obtained with Jiang and Wu's fifth-order WENO scheme [11] over two grids of sizes 48×30 and 96×60, respectively. The higher computational cost of the third-order reconstruction as compared to that of the fully discrete second-order scheme we used in [2] is compensated by the smaller number of grid points needed to resolve accurately the steep gradients that characterize the solution.

In the convective setup, the initial conditions and perturbation are the same as in the periodic setup, (5.5)–(5.7). In this case, the free outflow condition is applied also in the x-direction over the computational domain $[-\frac{L}{2}, \frac{L}{2}] \times [0, H]$, where $H = 20$ and $L = 55\pi$ with $L >> \lambda$—so chosen to allow the excitation to convect freely without disturbing the x-boundaries. The values of the bottom boundary of the computational

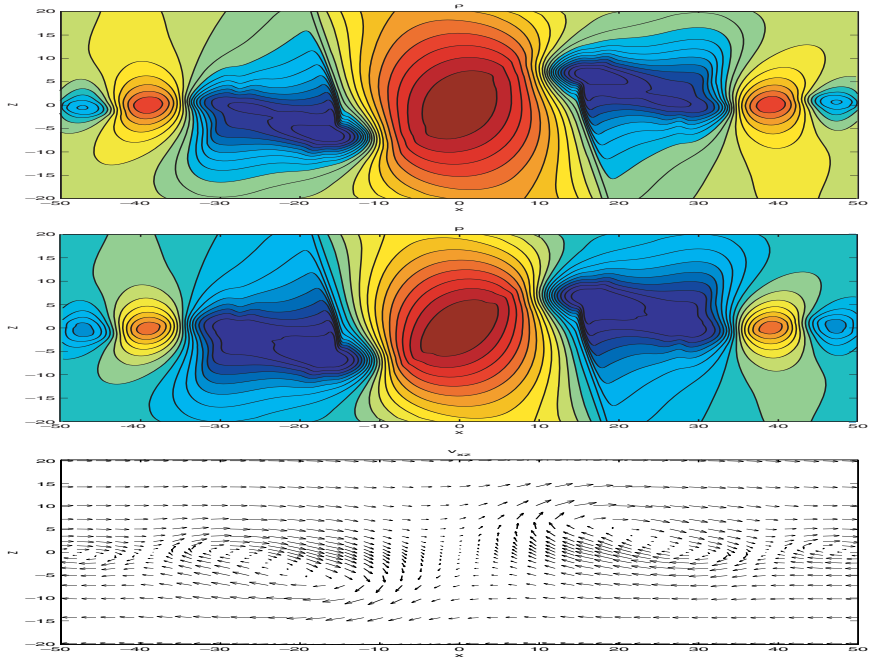

FIG. 5.3. *Solution of convective Kelvin–Helmholtz instability at* $t = 120$*, computed with third-order scheme on a* 792×72 *grid with* $c = 0.9$*. There are* 20 *contours for density and pressure, where darker colors indicate higher values. The density ranges from* 0.63 *to* 1.3*, the pressure ranges from* 0.20 *to* 0.85*, and the maximum value for the velocity is* 1.54*.*

domain, $z = 0$, are recovered by symmetry as in the periodic configuration. Figures 5.3 and 5.4 display the solution over the region $[-50, 50] \times [-20, 20]$ computed with 792×92 grid points over computational domain at $t = 120$ and $t = 145$, respectively. The values of the bottom half of the solution domain are recovered using the same symmetry conditions as used to reconstruct the bottom boundary.

5.3. Orszag–Tang MHD turbulence problem. This model considers the evolution of a compressible Orszag–Tang vortex system. The evolution of the vortex system involves the interaction between several shock waves traveling at various speed regimes [11, 28], which makes the problem useful to validate the robustness of numerical schemes. The initial data is given by

$$\rho(x, z, 0) = \gamma^2, v_x(x, z, 0) = -\sin z,\ v_z(x, z, 0) = \sin x,$$
$$p(x, z, 0) = \gamma, B_x(x, z, 0) = -\sin z, B_z(x, z, 0) = \sin 2x,$$

where $\gamma = 5/3$. With these data, the RMS values of the velocity and magnetic fields are both 1; the initial average Mach number is 1; and the average plasma beta is $10/3$. We solve the problem in $[0, 2\pi] \times [0, 2\pi]$ with periodic boundary conditions in both x- and z-directions. For this problem we implement the fourth-order reconstruction of section 3.2 and the SSP Runge–Kutta fourth-order ODE solver (3.20) using a uniform grid with 192×192 points and $c = 0.9$ in (5.4).

Figures 5.6, 5.7, and 5.8 display the solution of the Orszag–Tang vortex system at $t = 0.5, t = 2$, and $t = 3$, respectively. These simulations were performed with 192×192 grid points using the fourth-order, genuinely multidimensional, CWENO reconstruction of section 3.2 SSP Runge–Kutta solver (3.18)–(3.20). These results

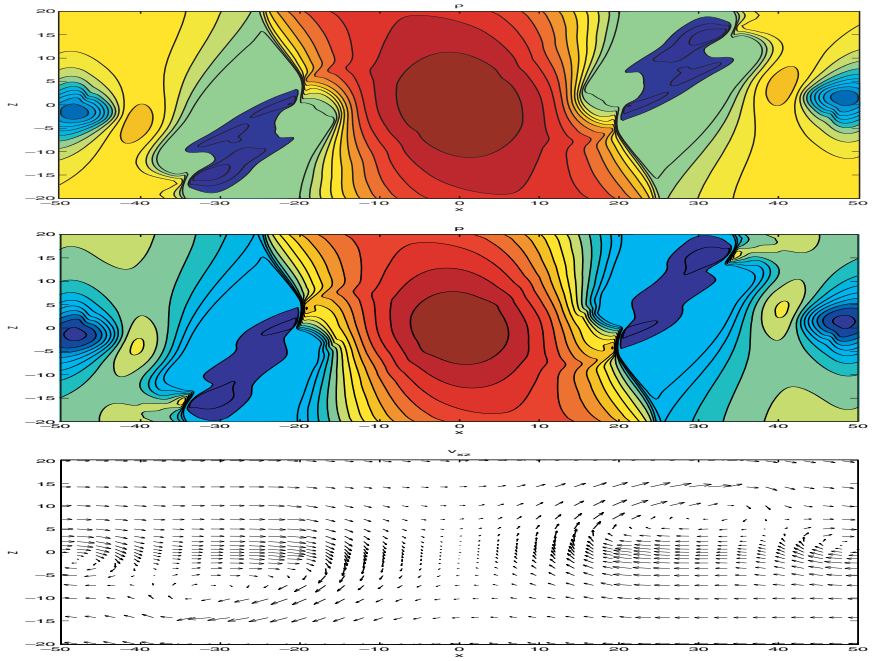

FIG. 5.4. *Solution of convective Kelvin–Helmholtz instability at* $t = 145$*, computed with third-order scheme on a* 792×72 *grid. There are* 20 *contours for density and pressure, where darker colors indicate higher values. The density ranges from* 0.43 *to* 1.3*, the pressure ranges from* 0.10 *to* 0.86*, and the maximum value for the velocity is* 1.94.

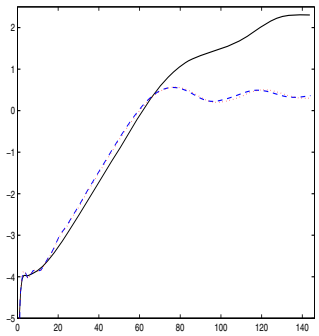

FIG. 5.5. *Time evolution of the total transverse kinetic energy,* $\log(\frac{1}{2}\int \rho v_z^2 dxdz)$*, integrated over* $[-L/2, L/2] \times [-H, H]$*, for both periodic and convective Kelvin–Helmholtz instability. The results for the periodic case with* 96×96 *and* 192×192 *grid points are represented by a dashed and a dotted curve, respectively. The convective configuration is represented by a solid line.*

demonstrate the ability of higher-order central schemes to resolve the shocks that the vortex system develops while maintaining the simplicity and ease of implementation typical of this *black-box* type of finite-difference schemes. We also note that similar results were obtained with the dimension-by-dimension third-order reconstruction and the Runge–Kutta solver (3.19) using a 288×288 mesh. The improved resolution of the fourth-order scheme allows us to compute accurate approximations using coarser grids than those required by lower-order schemes—consult Figures 5.5 and 5.9, for

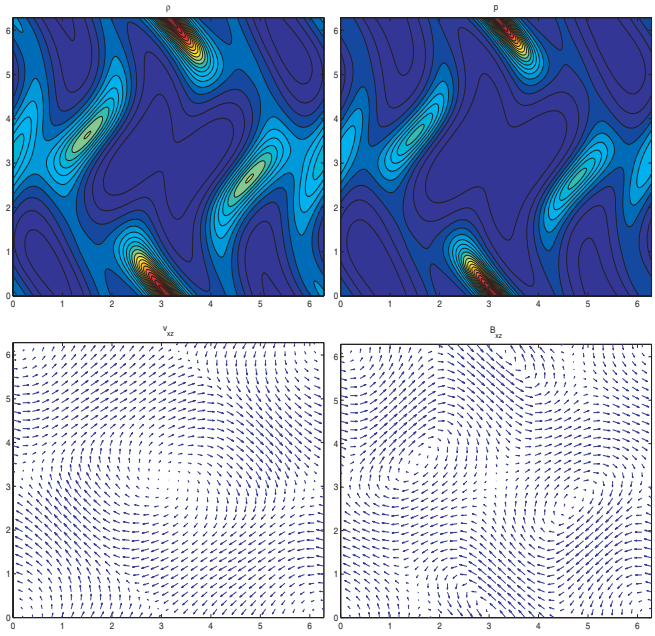

FIG. 5.6. *Fourth-order solution of Orszag–Tang MHD turbulence problem with a* 192×192 *uniform grid at* $t = 0.5$. *There are* 20 *contours for density and pressure, where darker colors indicate higher values. Density ranges from* 2.1 *to* 5.9, *pressure ranges from* 1.0 *to* 5.8. *The maximum values of* $|v|$ *and* $|B|$ *are* 1.6 *and* 1.6, *respectively.*

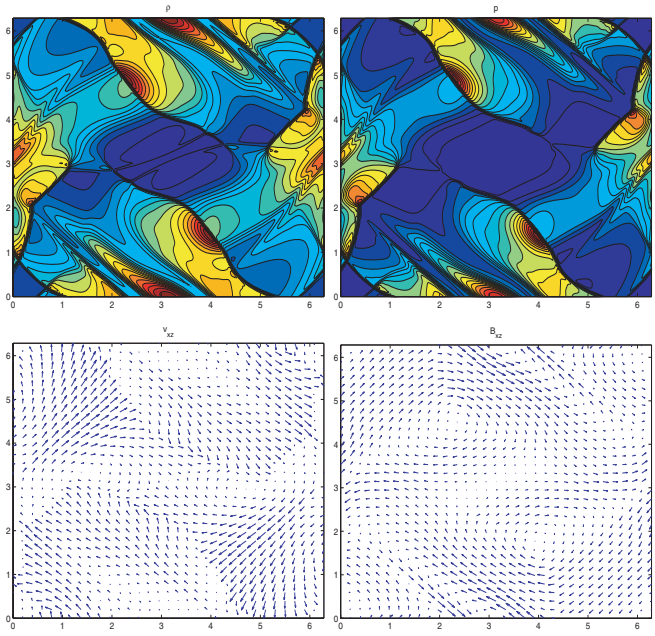

FIG. 5.7. *Fourth-order solution of Orszag–Tang MHD turbulence problem with a* 192×192 *uniform grid at* $t = 2$. *There are* 20 *contours for density and pressure, where darker colors indicate higher values. Density ranges from* 0.62 *to* 6.3, *pressure ranges from* 0.14 *to* 7.0. *The maximum values of* $|v|$ *and* $|B|$ *are* 1.6 *and* 2.8, *respectively.*

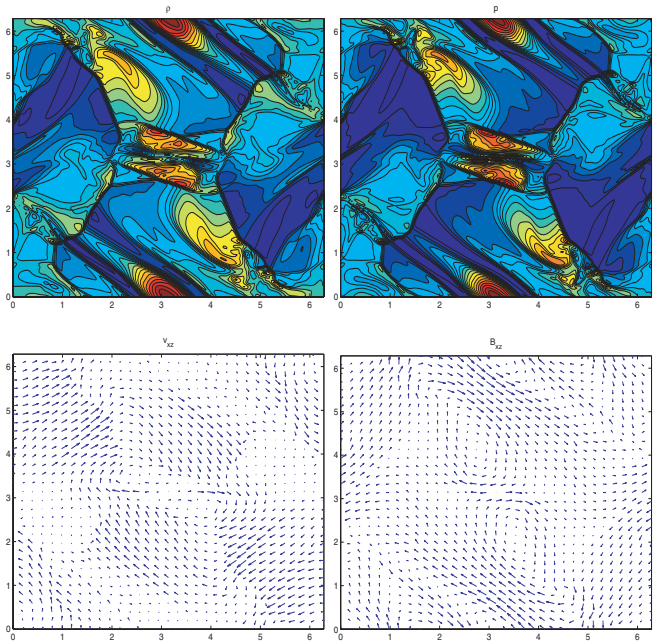

FIG. 5.8. *Fourth-order solution of Orszag–Tang MHD turbulence problem with a* 192×192 *uniform grid at* $t = 2$. *There are* 20 *contours for density and pressure, where darker colors indicate higher values. Density ranges from* 0.62 *to* 6.3, *pressure ranges from* 0.14 *to* 7.0. *The maximum values of* $|v|$ *and* $|B|$ *are* 1.6 *and* 2.8, *respectively.*

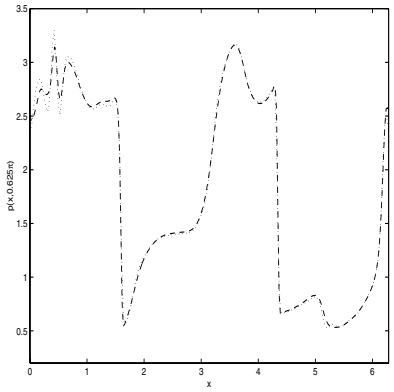

FIG. 5.9. *Pressure distribution along the line* $z = 0.625\pi$ *at* $t = 3$. *Dashed line corresponds to third-order approximation with* 288×288 *grid points and dotted line corresponds to fourth-order results computed with* 192×192 *gridpoints.*

example, thus reducing the computational cost of this type of simulation, an advantage that is more evident in higher space dimensions.

5.4. Interaction between a strong shock and a high-density cloud. This problem, introduced in [4], describes the disruption of a high-density cloud by a strong shock wave. The flow is simulated over the computational domain $[0, 1] \times [0, 1]$ with 256×256 cells and open boundary conditions. The ratio of specific heats is $\gamma = 5/3$

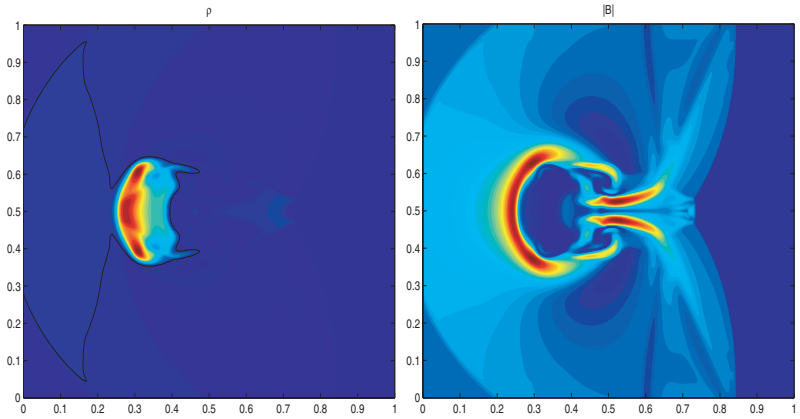

FIG. 5.10. *Third-order solution of the interaction between a strong shock and a high-density cloud obtained with a* 256×256 *uniform grid at* $t = 0.06$, $c = 0.5$. *Left: density; right: magnetic field,* $|B|$.

and the initial conditions are given by the two states,

(5.9)
$$(\rho, v_x, v_y, v_z, B_x, B_y, B_z, p)^\top = \begin{cases} (3.86859, 0, 0, 0, 0, -2.1826182, 2.1826182, 167.34)^\top & \text{for } x < 0.6, \\ (1, -11.2536, 0, 0, 0, 0.56418958, 0.56418958, 1)^\top & \text{for } x > 0.6, \end{cases}$$

separated by a discontinuity parallel to the z-axis at $x = 0.6$. To the right of the discontinuity there is a circular cloud of radius 0.15, centered at $x = 0.8$ and $z = 0.5$ with density $\rho = 10$ and $p = 1$. The solution we present in Figure 5.10 at $t = 0.06$ confirms the robustness of central schemes for highly superfast flows.

As in the case of the shock tube problem, the presence of discontinuities that affect only a particular component of the system—in this case a rotational discontinuity in the y component of the magnetic field—requires the careful choice of the smoothness indicators used in the calculation of the weights of the nonoscillatory reconstruction so as to prevent oscillations. Our numerical experiments suggest the use of the average of the smoothness indicators corresponding to the y-magnetic field and the density to determine the least oscillatory stencil for the evolution of all the conserved quantities.

6. Conclusions. The numerical schemes presented in this work and the results obtained with them complement those introduced in [2] and references therein and confirm the ability of this type of black-box solver to approximate the discontinuous solutions of ideal MHD equations accurately. The high-order semidiscrete schemes described in sections 2 and 3 retain the simplicity and ease of implementation of the fully discrete *staggered* methods while adding further advantages. As the limit of the reprojection of the staggered evolution of the cell averages, the semidiscrete formulation (2.17) requires only an estimate of the maximum local speeds of propagation to evolve the solution, avoiding any detailed knowledge of the eigen structure of (1.1)–(1.4) and, therefore, eliminating the need for Riemann solvers. The efficiency of the semidiscrete formulation is further enhanced by the larger time step that the implementation over nonstaggered grids yields and the wide range of reconstruction algorithms and ODE solvers available for its implementation. The use of these higher-order routines offers advantages that extend beyond the work presented here, in particular, the ability of

these schemes to compute accurate solutions over coarser grids and the possibility of applying the reconstruction algorithm dimension by dimension suggest these as an attractive alternative for schemes in higher space dimensions.

Our results also suggest a remarkable ability of central schemes to avoid any instability caused by the failure to satisfy the constraint $\nabla \cdot \mathbf{B} = 0$. All the results reported here have been calculated without any additional treatment for this constraint. Indeed, it can be shown that the magnetic field computed with the second-order staggered fully discrete schemes that lead to the semidiscrete formulation presented here satisfy the condition

$$\nabla \cdot \overline{\mathbf{B}}^{\,n+1}_{j+\frac{1}{2},k+\frac{1}{2}} = \nabla \cdot \overline{\mathbf{B}}^{\,n}_{j+\frac{1}{2},k+\frac{1}{2}}, \tag{6.1}$$

where $\overline{\mathbf{B}}^{\,n}_{j+\frac{1}{2},k+\frac{1}{2}}$ represents the cell average of the nonoscillatory polynomial reconstruction of the cell averages $\{\overline{\mathbf{B}}^{\,n}_{j+p,k+q}\}_{p,q=0,1}$.

Animations of the simulations presented in sections 4 and 5 and sample MHD codes are available online at http://www.math.lsa.umich.edu/∼jbalbas/MHD.

Acknowledgments. We thank C. Anderson of the UCLA Department of Mathematics for his advice in the computational aspects of this work and Dr. C-.C. Wu of the UCLA Department of Physics for his comments and suggestions.

REFERENCES

[1] J. Balbás, *Non-oscillatory Central Schemes for the Equations of Ideal Magnetohydrodynamics in One- and Two-Space Dimensions*, Ph.D. thesis, University of California, Los Angeles, May 2004.

[2] J. Balbás, E. Tadmor, and C.-C. Wu, *Non-oscillatory central schemes for one- and two-dimensional MHD equations.* I, J. Comput. Phys., 201 (2004), pp. 261–285.

[3] M. Brio and C. C. Wu, *An upwind differencing scheme for the equations of ideal magnetohydrodynamics*, J. Comput. Phys., 75 (1988), pp. 400–422.

[4] W. Dai and P. R. Woodward, *A simple finite difference scheme for multidimensional magnetohydrodynamical equations*, J. Comput. Phys., 142 (1998), pp. 331–369.

[5] S. Gottlieb, C.-W. Shu, and E. Tadmor, *Strong stability-preserving high-order time discretization methods*, SIAM Rev., 43 (2001), pp. 89–112.

[6] A. Harten, B. Engquist, S. Osher, and S. R. Chakravarthy, *Uniformly high-order accurate essentially nonoscillatory schemes.* III, J. Comput. Phys., 71 (1987), pp. 231–303.

[7] A. Harten, *High resolution schemes for hyperbolic conservation laws*, J. Comput. Phys., 49 (1983), pp. 357–393.

[8] G.-S. Jiang, D. Levy, C.-T. Lin, S. Osher, and E. Tadmor, *High-resolution nonoscillatory central schemes with nonstaggered grids for hyperbolic conservation laws*, SIAM J. Numer. Anal., 35 (1998), pp. 2147–2168.

[9] G.-S. Jiang and C.-W. Shu, *Efficient implementation of weighted ENO schemes*, J. Comput. Phys., 126 (1996), pp. 202–228.

[10] G.-S. Jiang and E. Tadmor, *Nonoscillatory central schemes for multidimensional hyperbolic conservation laws*, SIAM J. Sci. Comput., 19 (1998), pp. 1892–1917.

[11] G.-S. Jiang and C.-C. Wu, *A high-order WENO finite difference scheme for the equations of ideal magnetohydrodynamics*, J. Comput. Phys., 150 (1999), pp. 561–594.

[12] A. Kurganov and D. Levy, *A third-order semidiscrete central scheme for conservation laws and convection-diffusion equations*, SIAM J. Sci. Comput., 22 (2000), pp. 1461–1488.

[13] A. Kurganov and G. Petrova, *A third-order semi-discrete genuinely multidimensional central scheme for hyperbolic conservation laws and related problems*, Numer. Math., 88 (2001), pp. 683–729.

[14] A. Kurganov and E. Tadmor, *New high-resolution central schemes for nonlinear conservation laws and convection-diffusion equations*, J. Comput. Phys., 160 (2000), pp. 241–282.

[15] P. D. Lax, *Weak solutions of nonlinear hyperbolic equations and their numerical computation*, Comm. Pure Appl. Math., 7 (1954), pp. 159–193.

[16] D. Levy, G. Puppo, and G. Russo, *Central WENO schemes for hyperbolic systems of conservation laws*, Math. Model. Numer. Anal., 33 (1999), pp. 547–571.
[17] D. Levy, G. Puppo, and G. Russo, *A third order central WENO scheme for 2D conservation laws*, Appl. Numer. Math., 33 (2000), pp. 415–421.
[18] D. Levy, G. Puppo, and G. Russo, *A fourth-order central WENO scheme for multidimensional hyperbolic systems of conservation laws*, SIAM J. Sci. Comput., 24 (2002), pp. 480–506 (electronic).
[19] X.-D. Liu and E. Tadmor, *Third order nonoscillatory central scheme for hyperbolic conservation laws*, Numer. Math., 79 (1998), pp. 397–425.
[20] H. Nessyahu and E. Tadmor, *Nonoscillatory central differencing for hyperbolic conservation laws*, J. Comput. Phys., 87 (1990), pp. 408–463.
[21] S. A. Orszag and C. M. Tang, *Small-scale structure of two-dimensional magnetohydrodynamic turbulence*, J. Fluid Mech., 90 (1979), pp. 129–143.
[22] K. G. Powell, P. L. Roe, R. S Myong, T. Gombosi, and D. de Zeeuw, *An upwind scheme for magnetohydrodynamics*, in Proceedings of the AIAA 12th Computational Fluid Dynamics Conference, San Diego, 1995, pp. 661–674.
[23] C.-W. Shu, *Total-variation-diminishing time discretizations*, SIAM J. Sci. Statist. Comput., 9 (1988), pp. 1073–1084.
[24] C.-W. Shu, *Essentially non-oscillatory and weighted essentially non-oscillatory schemes for hyperbolic conservation laws*, in Advanced Numerical Approximation of Nonlinear Hyperbolic Equations, Lecture Notes in Math. 1697, Springer, Berlin, 1998, pp. 325–432.
[25] C.-W. Shu and S. Osher, *Efficient implementation of essentially nonoscillatory shock-capturing schemes.* II, J. Comput. Phys., 83 (1989), pp. 32–78.
[26] H.-Z. Tang and K. Xu, *A high-order gas-kinetic method for multidimensional ideal magnetohydrodynamics*, J. Comput. Phys., 165 (2000), pp. 69–88.
[27] B. van Leer, *Towards the ultimate conservative difference scheme.* V. *Second order sequel to Godunov method*, J. Comput. Phys., 32 (1979), pp. 101–136.
[28] C.-C. Wu and T. Chang, *Further study of the dynamics of two-dimensional MHD coherent structures—a large scale simulation*, J. Atmospheric Solar-Terrestrial Phys., 95 (2001), pp. 1447–1453.